Laser and Particle Beams (2016), *34*, 315–337.

doi:10.1017/S0263034616000185

Numerical simulation of Raman and Brillouin laser-pulse amplification in a magnetized plasma

MAGDI SHOUCRI
Institut de recherche d'Hydro-Québec (IREQ), Varennes, Québec, Canada J3X1S1
(Received 18 February 2016; Accepted 11 March 2016)

Abstract

We apply an Eulerian Vlasov code to study the amplification of an ultra-short seed pulse via stimulated Raman and Brillouin backscattering of energy from a long pump pulse, assumed at constant amplitude, in a plasma embedded in an external magnetic field. Detailed analysis of the spectra developed during the amplification process are presented, together with the evolution showing the pump depletion, accompanied by the counter-propagating seed-pulse amplification, compression and increased steepness of the waveform. In addition to the problem of the amplification of ultra-short seed pulses, there is an obvious academic interest in the study of problems of amplification of electromagnetic waves observed in many situations in laboratory plasmas and in the magnetosphere and other geophysical situations, such as in the environments of planets, where important variations in the presence and strength of magnetic fields are observed. The numerical code solves a one-dimensional relativistic Vlasov–Maxwell set of equations for a plasma in a magnetic field for both electrons and ions. We also apply the code to the problem of wakefield acceleration. The absence of noise in the Eulerian Vlasov code allows one to follow the evolution of the system with an accurate representation of the phase-space structures of the distribution functions.

Keywords: Laser beam; scattering; pulse amplification; wakefield; Eulerian Vlasov code

1. INTRODUCTION

Especial attention has been given recently, both theoretically and experimentally, to the idea of plasma-based laser amplifiers for their application to the direct amplification of ultra-short laser pulses. This process has been extensively examined in un-magnetized plasmas (see, for instance, Malkin *et al.*, 1999; Malkin & Fisch, 2014; Andreev *et al.*, 2006; Lancia *et al.*, 2010; Wang *et al.*, 2010; Trines *et al.*, 2011; Mourou *et al.*, 2012; Riconda *et al.*, 2013). This problem involves the interaction in a plasma of the ultra-short seed pulse with a long pump pulse, generally of low intensity, to amplify the counter-propagating seed-pulse intensity by several orders of magnitude. In this process, there is an energy transfer through stimulated scattering mediated by a resonant plasma wave, from the long pump electromagnetic (EM) wave with frequency and wavenumber $(\omega_{0P}, \vec{k}_{0P})$, to the initially low-intensity ultra-short seed pulse with frequency and wavenumber $(\omega_{0s}, \vec{k}_{0s})$. The resonant plasma wave can be either an electron plasma wave $(\omega_e, \vec{k}_e)$, as in the case of the stimulated Raman scattering (SRS), or an ion wave $(\omega_{ion}, \vec{k}_{ion})$ as in the case of the stimulated Brillouin scattering (SBS). The energy transfer requires the coupling of these waves through the momentum and energy conservation conditions $\vec{k}_{0P} = \vec{k}_{0S} + \vec{k}_{e,ion}$ and $\omega_{0P} = \omega_{0S} + \omega_{e,ion}$. For high energies, Raman and Brillouin processes might be even mixed (Lehmann *et al.*, 2012; Riconda *et al.*, 2013). Lehmann and Spaschek (2013), and Weber *et al.* (2013) have discussed the advantages and disadvantages of amplification of ultra-short laser pulses by Brillouin backscattering in plasmas, compared with Raman processes. Brillouin backscattering can amplify and compress pulses of extremely short duration.

It has recently been suggested that the addition of a magnetic field to the plasma can improve the confinement and the plasma performance, as suggested for instance by Grulke *et al.* (2015) for problems of wakefield accelerators. We present in this work some sample studies of the problem of plasma-based laser amplifiers when the plasma is embedded in an external magnetic field. Besides the academic importance of the problem and the laboratory interest of EM waves in many experimental situations, they are also observed in many geophysical situations, especially in our

Address correspondence and reprint requests to: M. Shoucri, Institut de recherche d'Hydro-Québec (IREQ), Varennes, Québec, Canada J3X1S1. E-mail: shoucri.magdi@ireq.ca

neighborhood in the environments of planets where the presence and strength of magnetic fields can have wide variations. The ionosphere is an upper atmospheric layer of plasmas, which results from the ionization of neutral atoms under the influence of solar radiation and energetic particles of the solar wind, and couples to the magnetosphere through strong field-aligned currents (see the review article by Briand, 2015). In the past several years, important theoretical and numerical simulation works have been published to understand the nonlinear growth of magnetospheric whistler-mode waves (see, for instance, the recent work by Summers *et al.*, 2013). Very low-frequency emissions have been artificially triggered in the magnetosphere by narrow whistler wave-trains of sufficient duration (Denavit & Sudan, 1975). See also the recent work of Tejero *et al.* (2015). It is not our intention to review these problems, we only point out the relevance of our work. We mention in addition the recent interest of imposing an axial magnetic field in inertial confinement fusion indirect-drive hohlraum plasmas, which could reduce SRS instabilities which affect coupling and cause preheat, and could improve laser–energy coupling in hohlraum targets (Montgomery *et al.,* 2015; Strozzi *et al.*, 2015).

Eulerian Vlasov codes have been successfully applied to the problem of the plasma-based laser-pulse amplifiers in the absence of an external magnetic field, for the problems of the backward SRS and SBS (Lehmann *et al.*, 2012, 2013; Shoucri *et al.,* 2014, 2015; Toroker *et al.*, 2014). They have also been successfully applied to the problem of wakefield accelerators in an un-magnetized plasma (Shoucri, 2008*b*). The results compared favorably to those obtained with the particle-in-cell (PIC) codes. In the PIC simulation results for seed-pulse amplification presented by Andreev *et al.* (2006) for instance, the length of the plasma amplifier had to be restricted due to the intrinsic numerical noise, because otherwise the pump would have been depleted by Brillouin scattering on the thermal noise, which is intrinsic in PIC simulations. Subsequently, Humphrey *et al.* (2013), studying the same problem, showed that the undesirable noise effects can be reduced by adding the collisions in the PIC simulations, as these damp the effects of thermal noise. The parameters of Humphrey *et al.* (2013) were used in a simulation with a Vlasov code by Shoucri *et al.* (2015), who showed the Vlasov code produced much more favorable results. Lehmann and Spatschek (2013) have also shown the difficulty of studying the SBS problems for laser-pulse amplification with PIC codes, because of the intrinsic numerical noise associated with these codes. The Eulerian Vlasov code we use for the present problem solves the one-dimensional (1D) relativistic Vlasov–Maxwell's equations for a plasma in a uniform external magnetic field for both electrons and ions. The code is fully kinetic along the direction of the magnetic field, and uses fluid equations in the direction normal to the external magnetic field. This code has been previously successfully applied for instance to the problem of beat-wave current drive (Ghizzo *et al.*, 1992). The code and the relevant equations are presented in Section 2. In Section 3, we test the code by studying the response of the code for a large amplitude perturbation. In Sections 4 and 5, we study respectively the SRS and SBS amplification of seed pulses, and in Section 6 we present a case of wakefield acceleration.

2. THE RELEVANT EQUATIONS OF THE EULERIAN VLASOV CODE AND THE NUMERICAL METHOD

The relevant equations for the problem we are studying have been presented previously (see, for instance, Appendix B in Ghizzo *et al.*, 1992 for more details). We rewrite these equations in order to fix the notation. Time t is normalized to the inverse electron plasma frequency ω_{pe}^{-1}, velocity and momentum are normalized respectively to the velocity of light c and to $M_e c$, where M_e is the electron mass, length is normalized to $l_0 = c\omega_{pe}^{-1}$, and the electric field is normalized to $E_0 = M_e \omega_{pe} c/e$. The 1D Vlasov equations for the electrons and ions distribution functions $f_{e,i}(x, p_{xe,i}, t)$ verify the relation:

$$\frac{\partial f_{e,i}}{\partial t} + \frac{p_{xe,i}}{m_{e,i}\gamma_{e,i}}\frac{\partial f_{e,i}}{\partial x} \mp (E_x + (\vec{u}_{\perp e,i} x \vec{B}_\perp)_x)\frac{\partial f_{e,i}}{\partial p_{xe,i}} = 0, \qquad (1)$$

where $\gamma_{e,i} \approx (1 + (p_{xe,i}/m_{e,i})^2)^{1/2}$. The upper sign in Eq. (1) is for the electron equation and the lower sign for the ion equation, and subscripts e and i denote electrons and ions, respectively. In our normalized units $m_e = 1$, and $m_i = M_i/M_e = 1836$ is the ratio of ion to electron masses. In this 1D model, the transverse velocity $\vec{u}_{\perp e,i}(x, t)$ is assumed non-relativistic and is calculated from a transverse "fluid" equation, but the kinetic features of the plasma are fully preserved along the external magnetic field in the longitudinal direction x. The transverse momentum $\vec{p}_{\perp e,i}(x, t) = m_{e,i}\vec{u}_{\perp e,i}$ is obtained through the introduction of the generalized canonical momentum defined by $\vec{P}_{\perp e,i}(x, t) = \vec{p}_{\perp e,i}(x, t) \mp \vec{a}_\perp(x, t)$ ($\vec{A}$ is the vector potential of the wave, and $\vec{a} = e\vec{A}/M_e c$ is the normalized vector potential), which obeys the "fluid" equation:

$$\left(\frac{\partial}{\partial t} + u_{xe,i}\frac{\partial}{\partial x}\right)\vec{P}_{\perp e,i} = \vec{P}_{\perp e,i} x \vec{\Omega}_{ce,i} \pm \vec{a}_\perp x \vec{\Omega}_{ce,i} \qquad (2)$$

with $u_{xe,i} = \int_{-\infty}^{+\infty} \frac{p_{xe,i}}{m_{e,i}\gamma_{e,i}} f_{e,i} d p_{xe,i}$.

$\vec{\Omega}_{ce,i} = \Omega_{ce,i}\vec{e}_x$, where $\Omega_{ce,i}$ is the electron (ion) cyclotron frequency, and $\vec{e}_x$ is the unit vector in the direction of the external magnetic field.

We adopt the Coulomb gauge $\nabla.\vec{a} = 0$, where the vector potential is in the perpendicular plane. The longitudinal electric field E_x is calculated either from the gradient of a potential $E_x = -\partial\varphi/\partial x$ or from the Ampére's law:

$$\frac{\partial E_x}{\partial t} = -J_x, \;\; J_x = \int_{-\infty}^{+\infty} \frac{p_{xi}}{m_i\gamma_i} f_i d p_{xi} - \int_{-\infty}^{+\infty} \frac{p_{xe}}{m_e\gamma_e} f_e d p_{xe}. \qquad (3)$$

https://doi.org/10.1017/S0263034616000185 Published online by Cambridge University Press

The transverse electric field $\vec{E}_\perp$ is calculated from the relations:

$$\vec{E}_\perp = -\frac{\partial \vec{a}_\perp}{\partial t}. \tag{4}$$

The transverse EM fields E_y, B_z and E_z, B_y for the circularly polarized wave obey Maxwell's equations. Defining $E^\pm = E_y \pm B_z$ and $F^\pm = E_z \pm B_y$ we have the following equations:

$$\left(\frac{\partial}{\partial t} \pm \frac{\partial}{\partial x}\right)E^\pm = -J_y \quad \left(\frac{\partial}{\partial t} \mp \frac{\partial}{\partial x}\right)F^\pm = -J_z, \tag{5}$$

which are integrated along their vacuum characteristics $x = \pm t$. In our normalized units, we have the following expressions for the normal current densities:

$$\vec{J}_\perp = \vec{J}_{\perp e} + \vec{J}_{\perp i};\ \vec{J}_{\perp e,i} = \mp n_{e,i}(x,t)\vec{u}_{\perp e,i}(x,t);\ n_{e,i}(x,t) = \int_{-\infty}^{+\infty} f_{e,i} dp_{xe,i}. \tag{6}$$

The numerical scheme applies a direct solution method of the Vlasov equation as a partial differential equation in phase space. This method has become an important method for the numerical solution of the Vlasov equation. In Eq. (1), $\gamma_{e,i} \approx (1 + (p_{xe,i}/m_{e,i})^2)^{1/2}$ is a function p_x only, which allows us to apply a time-splitting scheme with the separation of x and p_x variables by a method of fractional steps, as discussed for Eulerian Vlasov codes in several publications (Shoucri & Storey, 1986; Ghizzo *et al.*, 1990, 1992; Shoucri, 2008*a*).

3. TESTING THE CODE: PROPAGATION OF A LARGE AMPLITUDE WAVE

In this section, the response of the code is tested for large amplitude waves, in order to evaluate its precision and performance. Small amplitude perturbations of these waves will be used in Sections 4 and 5 for the SRS and SBS seed-pulse amplification problems.

3.1. The case of a forward scattering with a frequency of the laser pump $\omega_{0P} = 2.17$, the electron cyclotron frequency $\Omega_{ce} = 1.4$ and a vector potential for the pump $a_{0P} = 0.09$

We first test the code for a forward Raman scattering problem, where the forward injected large amplitude pump wave decays into another forward propagating wave and a plasma wave. We consider initially a Maxwellian plasma for the electrons and ions, with respective temperatures $T_e = 0.3$ keV and $T_i = 0.02$ keV. The ions do not play any role in the present physics, but have been included for the possible control of the small sheath at the edges. The linear dispersion relation for this problem is given by:

$$k^2 = \frac{\omega^2}{c^2}\left[1 - \frac{\omega_{pe}^2}{\omega(\omega \mp \Omega_{ce})}\right]. \tag{7}$$

The upper sign is for a right-hand circularly polarized wave (RCP), and the lower sign for a left-hand circularly polarized wave (LCP). The frequency of the EM wave is ω, and k the wavenumber. We consider a plasma such that the ratio of the electron cyclotron frequency Ω_{ce} to the electron plasma frequency ω_{pe} is $\Omega_{ce}/\omega_{pe} = 1.4$, and the ratio of the laser pump frequency $\omega = \omega_{0P}$ to the electron plasma frequency is $\omega_{0P}/\omega_{pe} = 2.17$. In the remaining of the text, we will use only normalized values and write $\Omega_{ce} = 1.4$ and $\omega_{0P} = 2.17$. The corresponding wavenumber for the RCP wave calculated from Eq. (7) equals to 1.376, and equals to 2.025 for the LCP.

For the case of the forward Raman scattering problem under consideration, we have a forward propagating circularly polarized laser beam entering the system at the left boundary ($x = 0$), and the forward propagating fields of the circularly polarized constant amplitude pump are given at $x = 0$ by $E^+ = 2E_{0P}\cos(\omega_{0P}t)$ and $F^- = 2E_{0P}\sin(\omega_{0P}t)$, where $\omega_{0P} = 2.17$ and E^+ and F^- are defined in Eq. (5). A characteristic parameter of high-power laser beams is the normalized vector potential or quiver momentum $\left|\vec{a}_\perp\right| = \left|e\vec{A}_\perp/M_e c\right| = a_0$, where $\vec{A}_\perp$ is the vector potential of the wave. For a circularly polarized wave $2a_0^2 = I\lambda_0^2/1.368 \times 10^{18}$, where I is the intensity in Wcm^{-2} and λ_0 the laser wavelength in microns. We take the amplitude of the vector potential of the pump to be $a_{0P} = 0.09$, which is sufficiently high to excite the possible Raman scattered modes without having to add a perturbation for a stimulation. We have in our normalized units $E_{0P} = \omega_{0P}a_{0P}$. We use a system of length $L = 800$. The number of grid points in space is $N = 120\,000$, so $\Delta x = \Delta t = 0.00667$. The extrema of momentum for the electrons are ± 0.6, with 1300 grid points used in velocity space.

Figure 1 shows the forward EM wave E^+ at the time of the arrival of the signal precursor at the right boundary at $t = 800$. The wave consists of the initial injected pump (see the constant amplitude pump at the left in Fig. 1), beating with the forward Raman scattered modes (these modes will be analyzed in Figs 4 and 5 below). The pump appears to deplete (see the lighter part of the graphic around $x = 600$) and then grow again (darker part of the graphic after $x = 700$). Figure 2

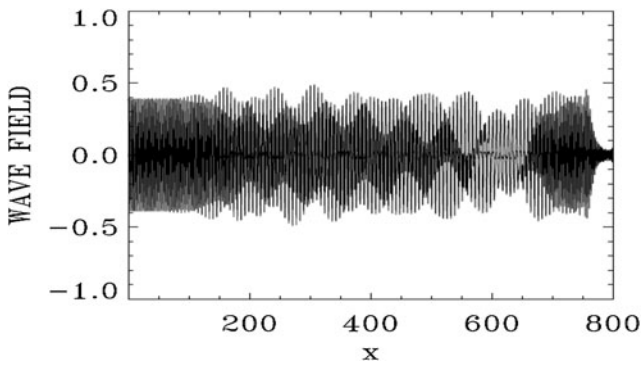

Fig. 1. The spatial profile of the forward wave E^+ at $t = 800$.

https://doi.org/10.1017/S0263034616000185 Published online by Cambridge University Press

shows the electron density and the electric field profiles at $t = 800$, and Figure 3 shows the phase-space contour plots of the electron distribution function at $t = 800$, at different position along the axis.

We present in Figure 4 the dominant spatial modes associated with the solution we present in Figures 1–3, by taking the Fourier transform in space for the forward wave E^+, the backward wave E^- and the longitudinal electric field E_x in the domain $x = (133, 570)$ at $t = 800$. Figure 5 presents the corresponding frequency spectra calculated by taking the temporal Fourier transform of the respective quantities in the time interval $t = (266, 704)$, recorded at the position $x = 200$. Figure 5 shows for E^+ the dominant frequency of the laser at $\omega_{0P} = 2.1704$, which is essentially the frequency 2.17 at which the pump is injected as we mentioned above. The wavenumber for E^+ in Figure 4 corresponding to this frequency is $k_{0P} = 2.0123$, in close agreement with the value of 2.025, which we calculated from Eq. (7) for $\omega_{0P} = 2.17$ for a LCP [note that in the present simulation we are injecting a large amplitude wave, and the temperature effect has been neglected in the derivation of Eq. (7)]. So the injection of a laser pump with $\omega_{0P} = 2.17$ at $x = 0$ has resulted in the excitation of a LCP wave with a wavenumber $k_{0P} = 2.0123$. We see in Figure 5 for the forward wave E^+ additional modes at frequencies 1.1786, 3.1622 and 4.154.

In free space, the forward wave E^+ and the backward wave E^- are decoupled. In a nonlinear medium like the plasma, there is a weak coupling between E^+ and E^- independent of the scattering process. This is the reason we observe in Figure 5 in the spectrum of E^- peaks at the frequencies 1.1786, 2.1704, and 3.1622 at a much lower level compared with the level observed in E^+, and in Figure 4 we observe in the spectrum of E^- peaks at the wavenumbers 0.967, 2.0123, and 3.076 at a much lower level compared with E^+.

The mode at $\omega_{0F} = 1.1786$ in the frequency spectrum of E^+ in Figure 5 results from the forward Raman scattering of the pump according to the selection rule $\omega_{0P} = \omega_{0F} + \omega_e$ (where ω_e is the excited plasma frequency normalized to the electron plasma frequency ω_{pe}), from which we get for the excited plasma frequency $\omega_e = \omega_{0P} - \omega_{0F} = 2.1704 - 1.1786 = 0.9918$, which is essentially the value of 1.00 we see in Figure 5 for the frequency spectrum of the electric field E_x (we note that the difference 1.00–0.9918 = 0.0082 is below the resolution of the Fourier transform, which is $d\omega = 0.0144$ in the present calculation). From Figure 4 the corresponding wavenumber of the forward scattered mode is $k_{0F} = 0.963$, in close agreement with the value of 0.965, we can calculate from Eq. (7) for $\omega_{0F} = 1.1786$. It obeys the selection rule for the forward Raman scattering $k_{0P} = k_{0F} + k_e$, from which $k_e = 2.0123 - 0.963 = 1.0493$, very close to the value of 1.063 calculated in Figure 4 in the spectrum of the electric field E_x. From the plasma wave dispersion relation $\omega_e^2 = \omega_{pe}^2 + 3k_e^2\upsilon_t^2$, written in normalized form as $\omega_e^2 = 1 + 3k_e^2(\upsilon_t^2/c^2)$, where υ_t is the thermal velocity given in our normalized units for a temperature T_e expressed in keV by $\upsilon_t/c = 0.04424\sqrt{T_e}$, and T_e is 0.3 keV in the present calculation. We get for the plasma frequency $\omega_e = 1.000$, which is the result we see in Figure 5 in the frequency spectrum of the electric field E_x. Note that the backward Raman scattering $k_{0P} = -k_{0F} + k_e$ is also possible, from which $k_e = 2.0123 + 0.967 = 2.979$, close to the harmonic at 3.191 in Figure 4. The corresponding frequency is $\omega_e = 1.00$, which obeys the selection rule $\omega_{0P} = \omega_{0F} + \omega_e$ as discussed above. But the mode at 0.967 in the spectrum of E^- in Figure 4 remained an order of magnitude smaller than the dominant modes in the spectrum of E^+. There is no other backward scattered mode excited by the pump.

Two more forward waves are excited for E^+, at the frequencies 3.1622 and 4.154 in Figure 5. This is essentially a cascade of LCP anti-Stokes resonance $\omega_{0A1} = 3.1622$ and $\omega_{0A2} = 4.154$. They obey the selection rule $\omega_{0A1} = \omega_{0P} + \omega_e$, from which $\omega_e = 3.1622 - 2.1704 = 0.9918$, which is essentially the value of 1.0 we see in the frequency spectrum of the electric field in Figure 5. In a similar way $\omega_{0A2} = \omega_{0A1} + \omega_e$, from which $\omega_e = \omega_{0A2} - \omega_{0A1} = 4.154 - 3.1622 = 0.9918$. For the corresponding wavenumbers for the anti-Stokes modes, we can calculate from the dispersion relation for the LCP wave in Eq. (7) for $\omega_{0A1} = 3.1622$ the wavenumber 3.05, very close to the value of $k_{0A1} = 3.076$ observed in Figure 4 for the spectrum of E^+ [note we are solving with

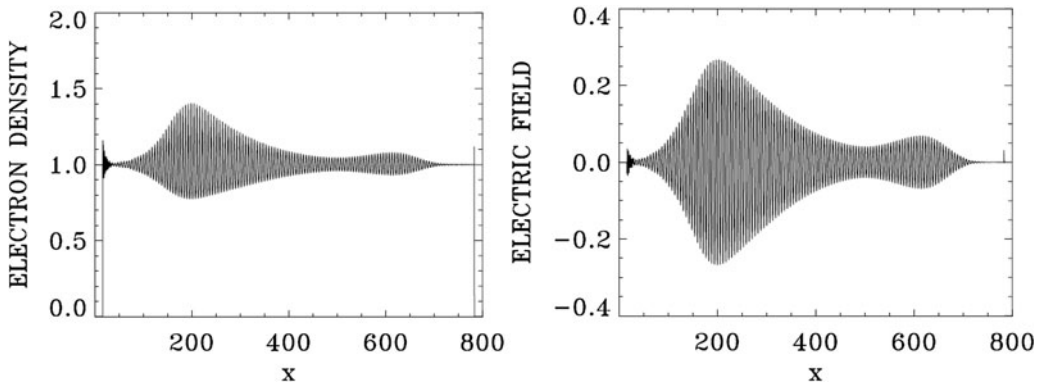

Fig. 2. Electron density and longitudinal electric field profiles at $t = 800$.

https://doi.org/10.1017/S0263034616000185 Published online by Cambridge University Press

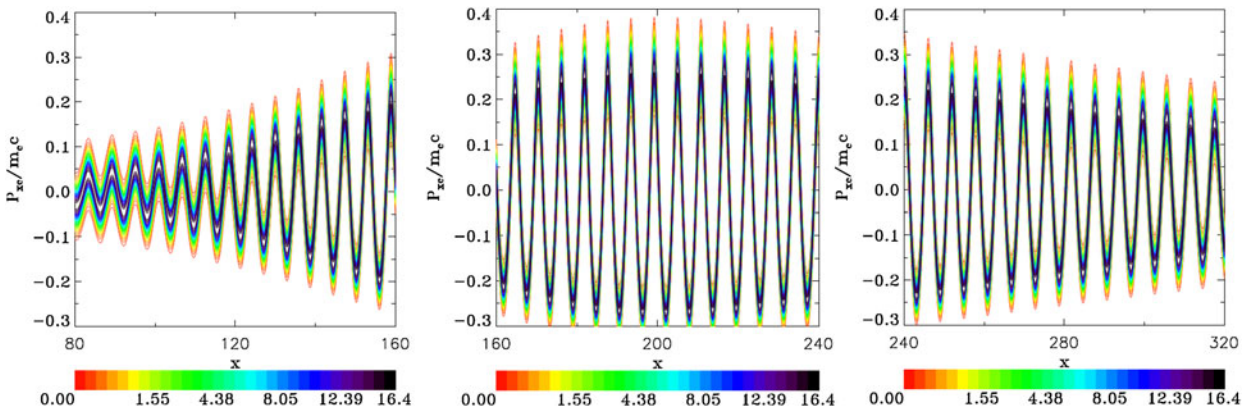

Fig. 3. Phase-space contour plots of the electron distribution function at different position in space at $t = 800$.

a large amplitude mode and in the presence of a thermal spread, while Eq. (7) is a linearized dispersion relation]. It also obeys the selection rule $k_{0P} = k_{0A1} + k_e$, from which the plasma mode wavenumber $k_e = k_{0P} - k_{0A1} = 3.076 - 2.0123 = 1.0637$, which is essentially the value we can read in Figure 4 in the electric field spectrum frame. In a similar way for $\omega_{0A2} = 4.154$, we get from Eq. (7) the wavenumber 4.063, very close to the value of $k_{0A2} = 4.139$ observed in Figure 4 for the spectrum of E^+. It obeys also the selection rule $k_{0A2} = k_{0A1} + k_e$, from which the plasma mode wavenumber $k_e = k_{0A2} - k_{0A1} = 4.139 - 3.076 = 1.063$, which is again the value we can read in Figure 4 in the electric field frame. We finally point out for the electric field in Figure 4 the harmonic structure of the wavenumber spectrum at 2.1273, 3.191, and 4.2834, and in Figure 5 the harmonic structure of the frequency spectrum at 1.998, 2.96, and 3.97. This is due to the large amplitude $a_{0P} = 0.09$ of the constant laser pump. Figure 2 shows large amplitude plasma waves.

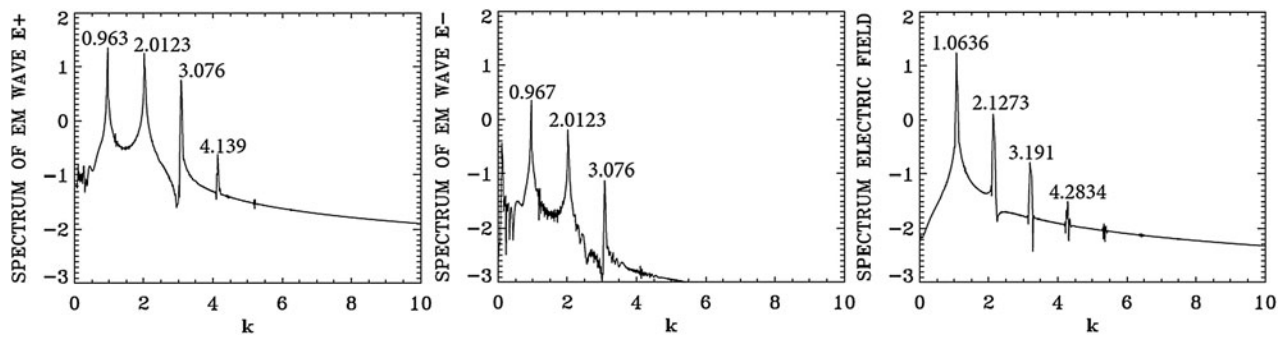

Fig. 4. Spatial Fourier transform in the domain $x = (133,570)$ of the forward wave E^+, the backward wave E^-, and the longitudinal electric field E_x at $t = 800$.

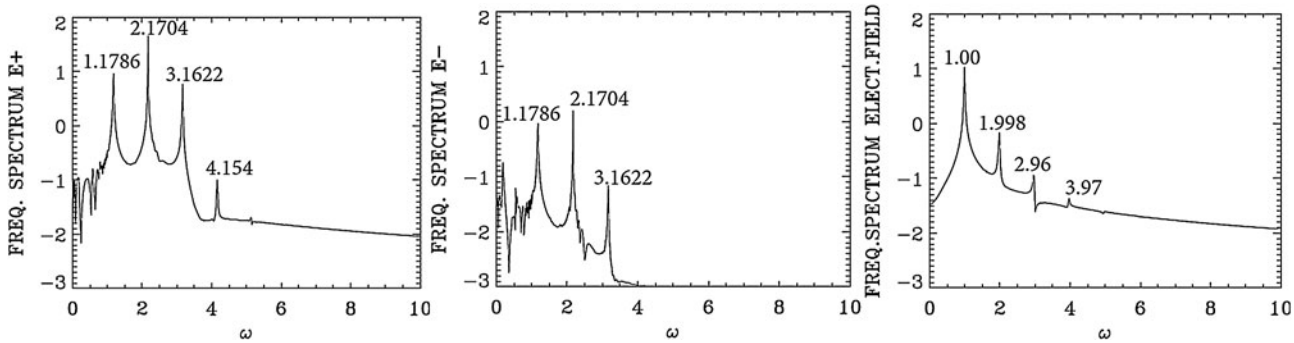

Fig. 5. Temporal Fourier transform, calculated in the time interval $t = (266,704)$, for the forward wave E^+, the backward wave E^-, and the longitudinal electric field E_x, taken at the position $x = 200$.

https://doi.org/10.1017/S0263034616000185 Published online by Cambridge University Press

3.2. The case of a forward scattering with a frequency of the laser pump $\omega_{0P} = 3.2$, the electron cyclotron frequency $\Omega_{ce} = 0.5$, and a vector potential for the pump $a_{0P} = 0.07$

We use the same parameters as in Section 3.1, except that for the pump laser beam we use a frequency $\omega_{0P} = 3.2$ and a vector potential $a_{0P} = 0.07$, and we consider a plasma such that the normalized electron cyclotron frequency $\Omega_{ce} = 0.5$. The corresponding wavenumber for the RCP wave calculated from Eq. (7) equals to 3.01, and equals to 3.062 for the LCP. Note the close values for these two wavenumbers for this lower value of $\Omega_{ce} = 0.5$. Details of the injection of the pump at $x = 0$ are the same as in the previous section.

Figure 6 shows the forward EM wave E^+ at $t = 533.3$, and at the time of the arrival of the signal precursor at the right boundary at $t = 800$. The wave consists of the initial injected pump (see the constant amplitude pump at the left), beating with the forward scattered modes, which are excited without perturbation due to the high amplitude of the pump $a_{0P} = 0.07$ (these modes will be analyzed in Figures 7 and 8 below). The pump appears to deplete (see the lighter parts of the graphic) and then grow again (darker part of the graphic). These oscillations appear to be more regular at $t = 533.3$, with respect to what is presented at $t = 800$. Spatial Fourier transforms for E^+, E^-, and the longitudinal electric field at the early stage at $t = 533.3$ are presented in Figure 7, and provides the information about the modes which develop at this early stage. These transforms are calculated by Fourier transforming the signal in the interval $x = (67,504)$ at $t = 533.3$. Figure 8 presents the corresponding frequencies calculated by a temporal Fourier transform of the signal at the position $x = 200$, in the time interval $t = (233,452)$.

Figure 8 shows the dominant frequency for E^+ calculated by the code is at $\omega_{0P} = 3.205$, which is essentially the frequency 3.2 at which the pump is injected as we mentioned above. The wavenumber for E^+ in Figure 7 corresponding to this frequency is $k_{0P} = 3.061$, in agreement with the value of 3.061 which can be calculated from Eq. (7) for $\omega_{0P} = 3.2$ for a LCP. So the injection of a laser pump with $\omega_{0P} = 3.2$ at $x = 0$ has resulted in the excitation of a LCP wave with $k_{0P} = 3.061$. We see in Figure 8 for the forward wave E^+ additional modes at frequencies 2.199, 4.197, and 5.19. The mode at $\omega_{0F} = 2.199$ results from the forward Raman scattering of the pump according to the selection rule $\omega_{0P} = \omega_{0F} + \omega_e$, from which we get for the excited plasma frequency $\omega_e = \omega_{0P} - \omega_{0F} = 3.205 - 2.199 = 1.006$, which is essentially the value of 1.00 we see in Figure 8 for the frequency spectrum of the electric field. From Figure 7 the corresponding wavenumber of the forward scattered mode is $k_{0F} = 2.012$, in close agreement with the value of 2.006, which can be calculated from Eq. (7) for $\omega_{0F} = 2.199$. It obeys the selection rule for the forward Raman scattering $k_{0P} = k_{0F} + k_e$, from which $k_e = 3.061 - 2.012 = 1.049$, which is essentially the value calculated in Figure 7 in the electric field spectrum. From the plasma wave dispersion relation $\omega_e^2 = 1 + 3k_e^2(\upsilon_t^2/c^2)$, where υ_t is the thermal velocity given in our normalized units by $\upsilon_t/c = 0.04424\sqrt{T_e}$, and T_e is 0.3 keV in the present calculation. We get for the plasma frequency $\omega_e = 1.00$ for $k_e = 1.049$, which is the result we see in Figure 8 in the frequency spectrum of the longitudinal electric field E_x.

As explained in the previous section, there is a weak coupling between E^+ and E^- in the nonlinear medium independent of the scattering process. This is the reason we observe in Figure 8 in the spectrum of E^- peaks at the frequencies 2.199, 3.205, and 4.197 at a much lower level compared with E^+, and in Figure 7 we observe in the spectrum of E^- peaks at the wavenumbers 0.948, 2.012, 3.061, and 4.11 at a much lower level compared with E^+.

In Figure 7, the pump E^+ at the wavenumber $k_{0P} = 3.061$ and the plasma mode at $k_e = 1.049$ give the anti-Stokes mode at $4.11 = 3.061 + 1.049$, which is the value observed in Figure 7 in the spectrum of E^+. The corresponding frequencies in Figure 8 are $3.20 + 1.00 = 4.20$ (very close to the peak at 4.197 we see in Figure 8). Note that the wavenumber calculated from Eq. (7) for a frequency of 4.197 is 4.09, very close to the value of 4.11 we see in Figure 7. We also note in Figure 7 a second cascade of anti-Stokes in the spectrum of E^+ at $4.11 + 1.049 = 5.159$, which is the peak appearing in 5.15 in Figure 7. And the corresponding frequency resonance for this second anti-Stokes cascade in the spectrum of E^+ in

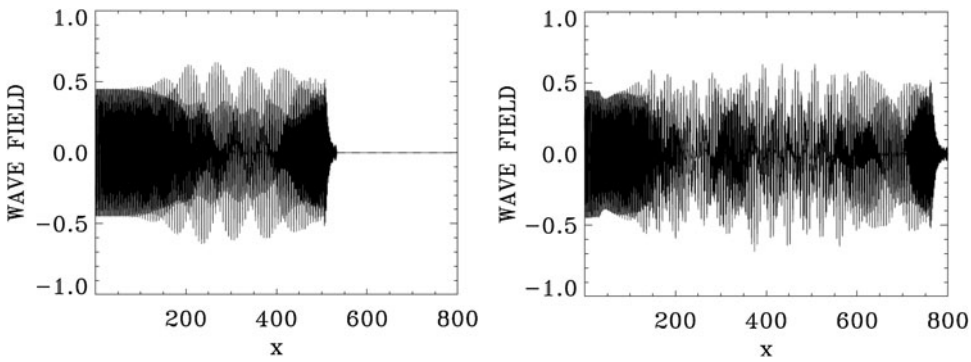

Fig. 6. The forward wave E^+ at $t = 533.3$ (left frame) and $t = 800$ (right frame).

https://doi.org/10.1017/S0263034616000185 Published online by Cambridge University Press

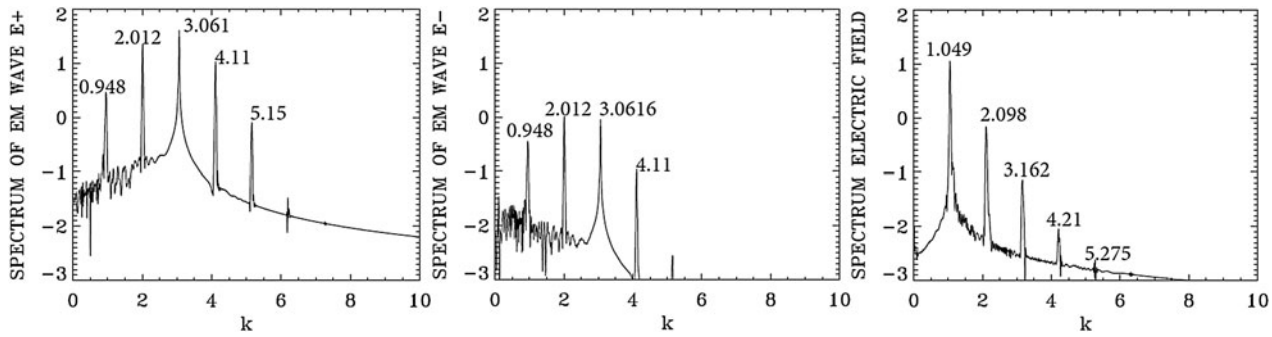

Fig. 7. Spatial Fourier transform in the domain $x = (67,504)$ of the forward wave E^+, the backward wave E^-, and the longitudinal electric field E_x at $t = 533.3$.

Figure 8 is 4.197 + 1.00 = 5.197, very close to the value of 5.19 we see in Figure 8. We see also in Figure 7 for E^+ a re-scattering in the forward direction $2.012 = 0.948 + k_e$, from which the wavenumber of the plasma mode $k_e = 1.064$, very close to the value of 1.049 in the spectrum of the electric field in Figure 7, and the corresponding frequencies for this re-scattering in Figure 8 are at 2.199 and 1.20 (the small peak not marked in Figure 8), from which the selection rule $2.199 = 1.20 + \omega_e$, that is, $\omega_e = 0.999$ which is essentially the value of 1.00 we see in Figure 8 in the spectrum of the longitudinal electric field. Indeed for $k_e = 1.064$, the relation $\omega_e^2 = 1 + 3k_e^2(\upsilon_t^2/c^2)$ gives $\omega_e = 1.0$. From these results, we see that there is no backward scattered wave excited by the laser pump at this stage at $t = 533.3$.

We present in Figure 9 the plots of the electron density at $t = 533.3$ and 800. Figure 10 presents the plots of the longitudinal electric field at $t = 533.3$ and 800. We now study the wavenumber spectra at a later time at $t = 800$. Figure 11 presents the frequency spectra for the signal recorded at $x = 200$, in the time interval $t = (233,671)$. The frequency spectrum of E^+ shows the dominant frequencies presented in Figure 8, with the pump frequency appearing at $\omega_{0P} = 3.205$, which is essentially the frequency 3.2 at which the pump is injected as we mentioned above. The wavenumber spectra response in

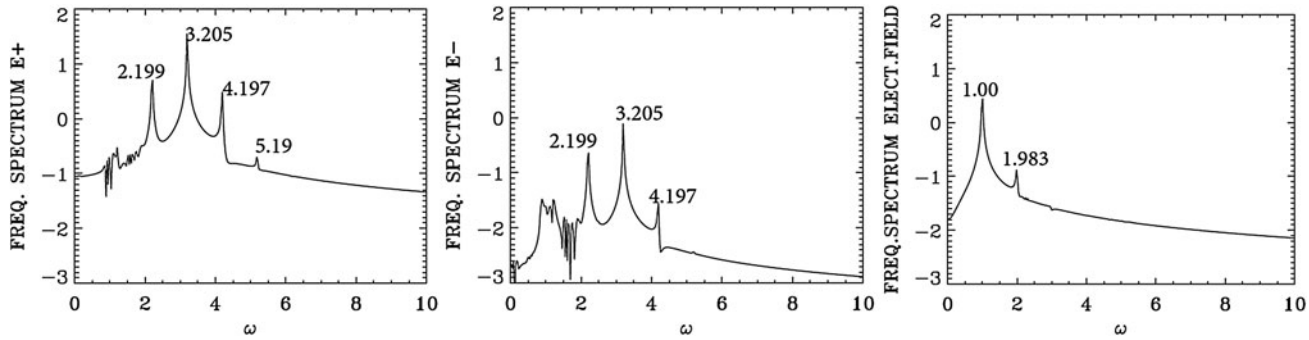

Fig. 8. Temporal Fourier transform, calculated in the time interval $t = (233,452)$, for the forward wave E^+, the backward wave E^-, and the longitudinal electric field E_x, taken at the position $x = 200$.

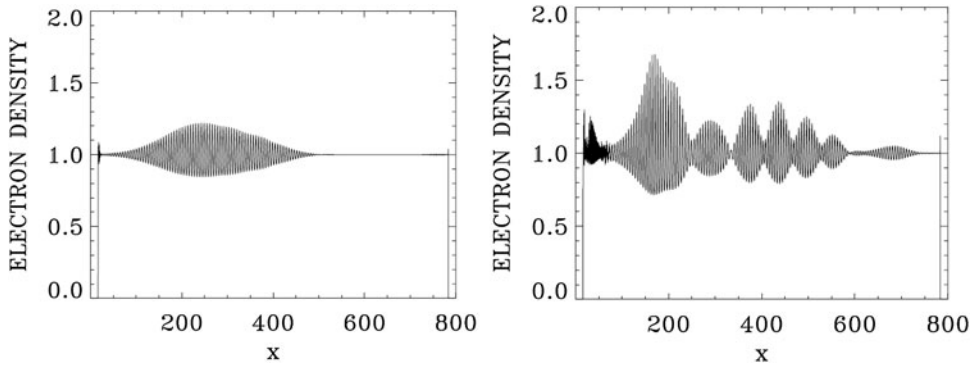

Fig. 9. The electron density at $t = 533.3$ (left frame) and $t = 800$ (right frame).

https://doi.org/10.1017/S0263034616000185 Published online by Cambridge University Press

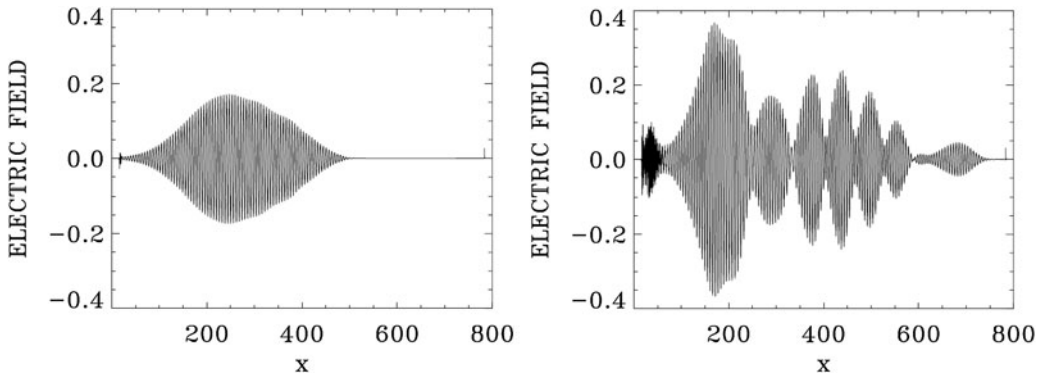

Fig. 10. The longitudinal electric field at $t = 533.3$ (left frame) and $t = 800$ (right frame).

the domain $x = (100,537)$ are presented in Figure 12 at $t = 800$, slightly different from what we present in Figure 7. The wavenumber for E^+ in Figure 12 corresponding to the frequency $\omega_{0P} = 3.205$ is $k_{0P} = 3.061$, in agreement with the value of 3.061 which can be calculated from Eq. (7) for $\omega_{0P} = 3.2$ for a LCP. The forward re-scattered mode at 1.20 in Figure 11, which results from the forward re-scattering of the mode at the frequency 2.199 according to the selection rule $2.199 = \omega_{0F} + 1.00$, from which $\omega_{0F} = 1.199$, as discussed in Figure 8 in the spectrum of E^+, is now more developed in Figure 11. The wavenumber for E^+ in Figure 12 corresponding to frequency $\omega_s = 1.2$ is at $k = 0.891$, very close with the value of 0.8568, which can be calculated from Eq. (7) for $\omega_s = 1.2$ for a LCP. The peaks in Figure 11 are the same frequencies as in Figure 8, although more developed, and we note in Figure 11 the important harmonic response for the plasma frequency in the spectrum of the longitudinal electric field. The wavenumbers response to these frequencies in Figure 12 shows the spectra, which are broad around the peaks, in contrast to what we see

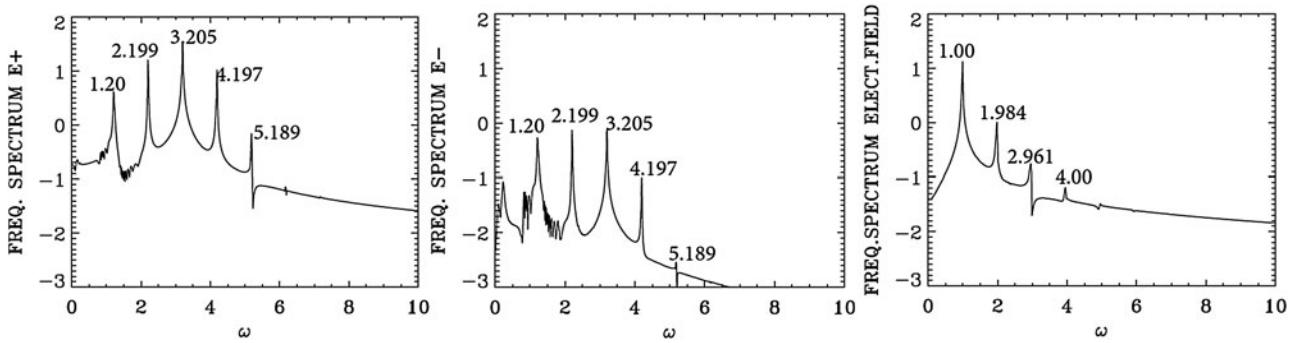

Fig. 11. Temporal Fourier transform, calculated in the time interval $t = (233,671)$, for the forward wave E^+, the backward wave E^-, and the longitudinal electric field E_x, taken at the position $x = 200$.

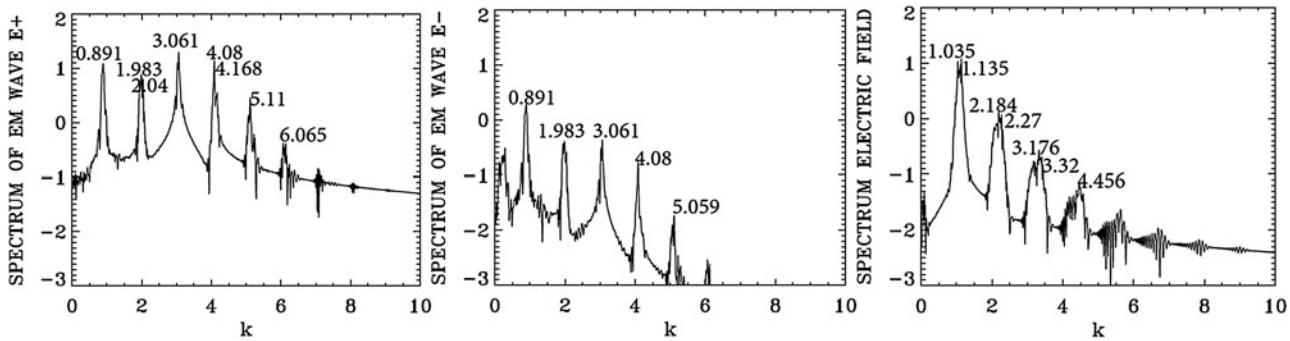

Fig. 12. Spatial Fourier transform in the domain $x = (100,537)$ of the forward wave E^+, the backward wave E^-, and the longitudinal electric field E_x, at $t = 800$.

https://doi.org/10.1017/S0263034616000185 Published online by Cambridge University Press

in Figure 7. In the present nonlinear stage, this points to a coupling with a RCP wave, which results in the broadening of the peaks in Figure 12. At the frequency 3.2 in Figure 11, Eq. (7) gives a wavenumber response of 3.061 for the LCP wave, and 3.01 for the RCP wave, well within the broad spectrum we see in Figure 12 around 3.061. Similarly at the frequency of 2.2 in Figure 11, Eq. (7) gives the wavenumber value of 2.006 for the LCP mode, and 1.90 for the RCP mode, within the broad peak we see around (1.983,2.04) in Figure 12. In addition to the scattering previously discussed in Figures 7 and 8 for the LCP modes, we have now couplings with the RCP modes, which explain the broadening we see in the wavenumber spectra in Figure 12. The frequency of the anti-Stokes resonance at 4.197 in Figure 11 leads from Eq. (7) to a wavenumber response at 4.09 for the LCP wave and 4.06 for the RCP wave. This RCP wave at wavenumber 4.06 can couple to the RCP wave at 3.01 to give the plasma response at the wavenumber 4.06–3.01 = 1.05, well within the broad peak we see in Figure 12 for the plasma response of the electric field around (1.035,1.135). Similarly the RCP wave at the wavenumber of 3.01 can couple with the RCP wave at the wavenumber 1.9 to give the plasma response in the electric field spectrum at the wavenumber 3.01–1.9 = 1.11, well within the broad peak around (1.035,1.135) we see in Figure 12 for the longitudinal electric field. So the broad peaks for the wavenumber harmonics in the spectrum of the longitudinal electric field in Figure 12 result from the coupling of LCP and RCP waves excited due to the high amplitude pump E^+. Finally, we observe in the spectrum of E^- in Figures 11 and 12 peaks at the same frequencies and wavenumbers, but at a much lower level compared with E^+, due to the coupling in the nonlinear plasma medium as explained before. However, there is no backward scattered wave excited by the laser pump.

Finally, we present in Figure 13 the phase-space contour plots for the electron distribution function at $t = 800$, from $x = 240$ to 480. Between $x = 400$ and 440 we note the presence of about seven peaks, which leads to a wavelength of about 40/7 or 5.7. We get a close result if we consider the dominant wavenumber of the longitudinal electric field in Figure 12 at the average peak of 1.1, which leads to a wavelength $\approx 2\pi/1.1 = 5.7$.

4. THE CASE OF THE BACKWARD RAMAN AMPLIFICATION OF A SEED PULSE

We consider a plasma where the electron cyclotron frequency is $\Omega_{ce} = 1.4$, and the laser pump frequency is $\omega_{0P} = 3.2$. From Eq. (7), the corresponding wavenumber for a LCP wave is 3.089, and for a RCP wave the corresponding wavenumber is 2.909. For the seed pulse, we take the frequency $\omega_{0S} = 2.17$, which is the frequency we used in Section 3.1, and which from Eq. (7) corresponds to a wavenumber 2.025 for the LCP wave and 1.376 for the RCP wave.

The length of the system is $L = 600$. There is a uniform plasma slab of length $L_p = 572.5$, and a vacuum region of length $L_{vac} = 12.5$ on both sides of the slab, and a transition from vacuum to the plasma at the plasma edge of length $L_{edge} = 15$ on both sides, for a total length of 600. $N = 120\,000$ grid points are used in space, and in our normalized units $\Delta x = \Delta t = 0.005$. The extrema of momentum for the electrons are ± 0.5, and with 1000 grid points in velocity space, we have a grid size of $\Delta\upsilon = 10^{-3}$. Ions were allowed to move in order to fix the small sheath at the edge of the plasma, but have otherwise no effect on the results. The units of time ω_{pe}^{-1} and space c/ω_{pe} we use can be easily translated into units of ω_{0P}^{-1} and c/ω_{0P} by dividing them by the factor, $\omega_{0P}/\omega_{pe} = 3.2$.

For the case considered for the problem of the Raman amplification of a seed pulse, we have a forward-propagating circularly polarized laser beam entering the system at the left boundary ($x = 0$) at the $t = 0$, and the forward-propagating fields of the circularly polarized constant amplitude pump are given at $x = 0$ by $E^+ = 2E_{0P}\cos(\omega_{0P}t)$ and $F^- = 2E_{0P}\sin(\omega_{0P}t)$, E^+ and F^- are defined in Eq. (5). We have in our normalized units $E_{0P} = \omega_{0P}a_{0P}$. The pump precursor reaches the right boundary $x = 600$ at $t = 600$, since in our normalized units $x = t$. The seed pulse is injected

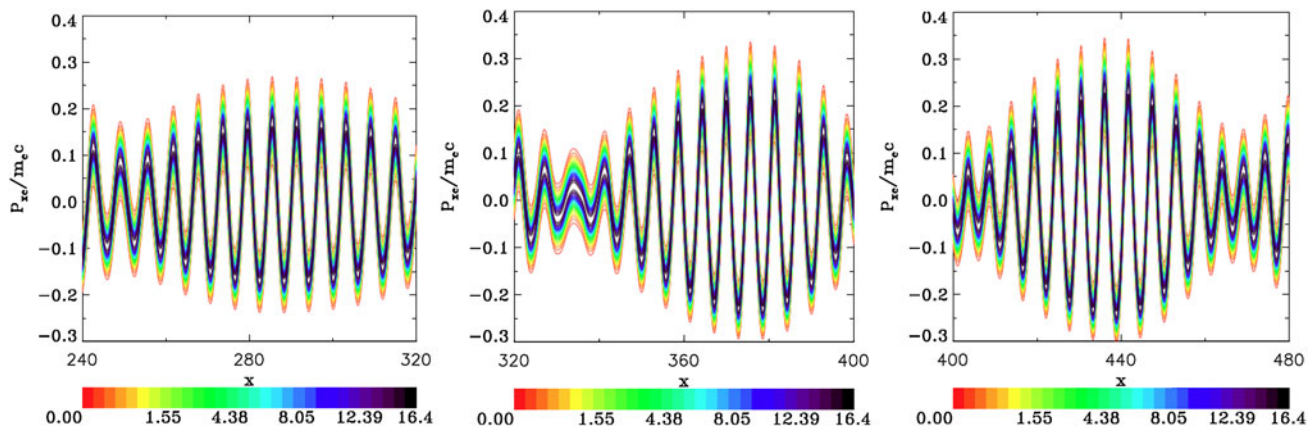

Fig. 13. Phase-space contour plots of the electron distribution function at different position in space at $t = 800$.

https://doi.org/10.1017/S0263034616000185 Published online by Cambridge University Press

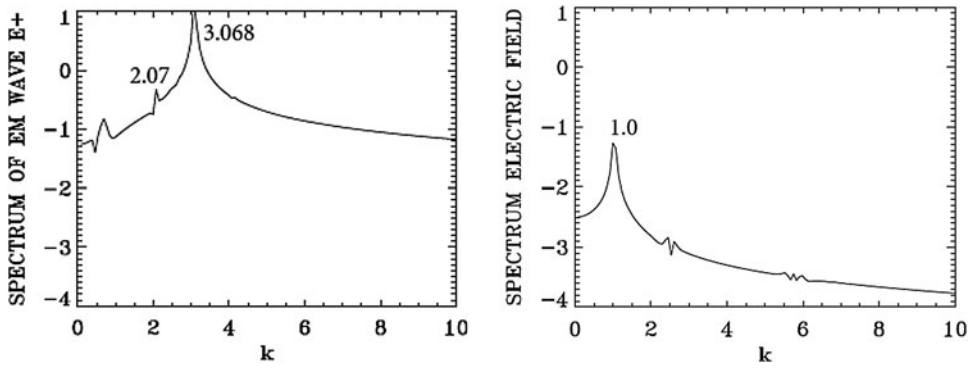

Fig. 14. Spatial Fourier transform of the forward wave E^+ and the electric field E_x in the domain $x = (450,532)$ at $t = 600$.

at the right boundary $x = 600$ in the backward direction just before the arrival of the pump, in the time interval $540 < t < 600$, with $E^- = 2E_{0S}P_r(t)\cos(\omega_{0S}(t-540))$ and $F^+ = -2E_{0S}P_r(t)\sin(\omega_{0S}(t-540))$, with $E_{0S} = \omega_{0S}a_{0S}$. We take the amplitude of the vector potential of the pump and the seed to be $a_{0P} = a_{0S} = 0.04$. The initial distribution functions for electrons and ions are Maxwellian with temperatures $T_e = 0.35$ keV for the electrons and $T_i = 0.1$ keV for the ions. The shape factor $P_r(t)$ for the injected seed pulse has a Gaussian time dependence:

$$P_r(t) = \exp(-0.5(t-570)/t_p)^2;\ 540 < t < 600;\ t_p = 10. \quad (8)$$

The backward-propagating seed pulse behaves as a Gaussian pulse in time for $540 < t < 600$, which reaches its peak at $t = 570$, and has completely penetrated the plasma at $t = 600$, that is, at the time the pump precursor reaches the right boundary.

We present in Figure 14 the wavenumber spectra in the domain $x = (450, 532)$ at $t = 600$, before the arrival of the injected backward seed pulse in this domain, which at $t = 600$ has penetrated to reach the point $x = 540$, according to the discussion of the previous paragraph. The spectrum for the pump E^+ shows a dominant peak at $k_{0P} = 3.068$, very close to the value of 3.089 calculated from the dispersion relation in Eq. (7) for the LCP wavenumber response to the injected pump at $\omega_{0P} = 3.2$. It shows also a small forward scattered wave at 2.07, satisfying $k_{0P} = 2.07 + k_e$, from which we have for the plasma wave $k_e = 3.068 - 2.07 = 0.998$, which is essentially the value $k_e \approx 1$ we see in Figure 14. We see indeed a low intensity and large peak in Figure 14 around the value of 1.0 in the spectrum of the longitudinal electric field. Due to the lower amplitude level of the laser pump ($a_{0P} = 0.04$) in the present calculation, the level of the excited forward scattered wave remained very low. As discussed in the previous section, the spectrum of E^- shows essentially the same peaks as for E^+ due to the coupling in the nonlinear plasma medium, but remained much lower than E^+. No backward scattered wave developed.

We present in Figure 15 the frequency spectrum corresponding to the results presented in Figure 14. The temporal Fourier transform of E^+ is taken at the position $x = 450$ in the time interval $t = (545,632)$, before the arrival of the backward seed pulse injected at the right of the domain. The peak frequency of the injected pump E^+ at the frequency 3.2 is appearing in Figure 15 at 3.22. The frequency of the forward scattered mode appears at 2.147 [the corresponding wavenumber calculated from the dispersion relation in Eq. (7) gives for the LCP wave the value of 2.00, close to the

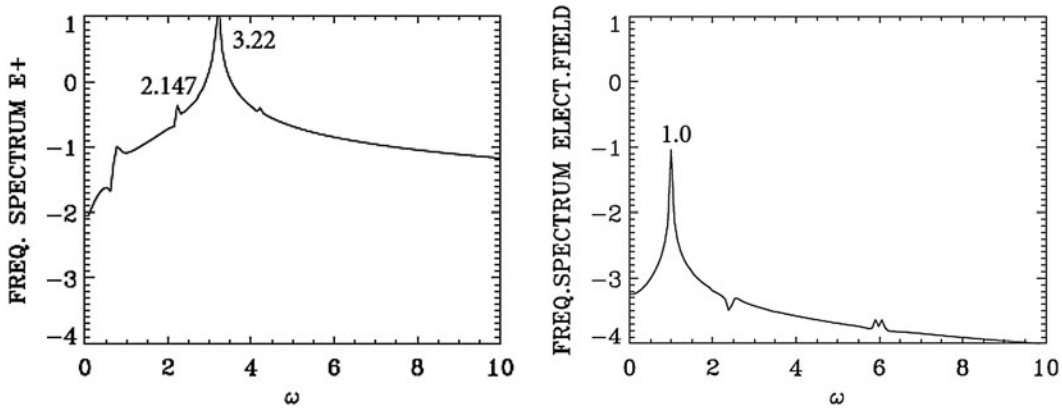

Fig. 15. Temporal Fourier transform of the forward wave E^+ (full curve) and the electric field E_x for time interval $t = (545,632)$ at the position $x = 450$.

https://doi.org/10.1017/S0263034616000185 Published online by Cambridge University Press

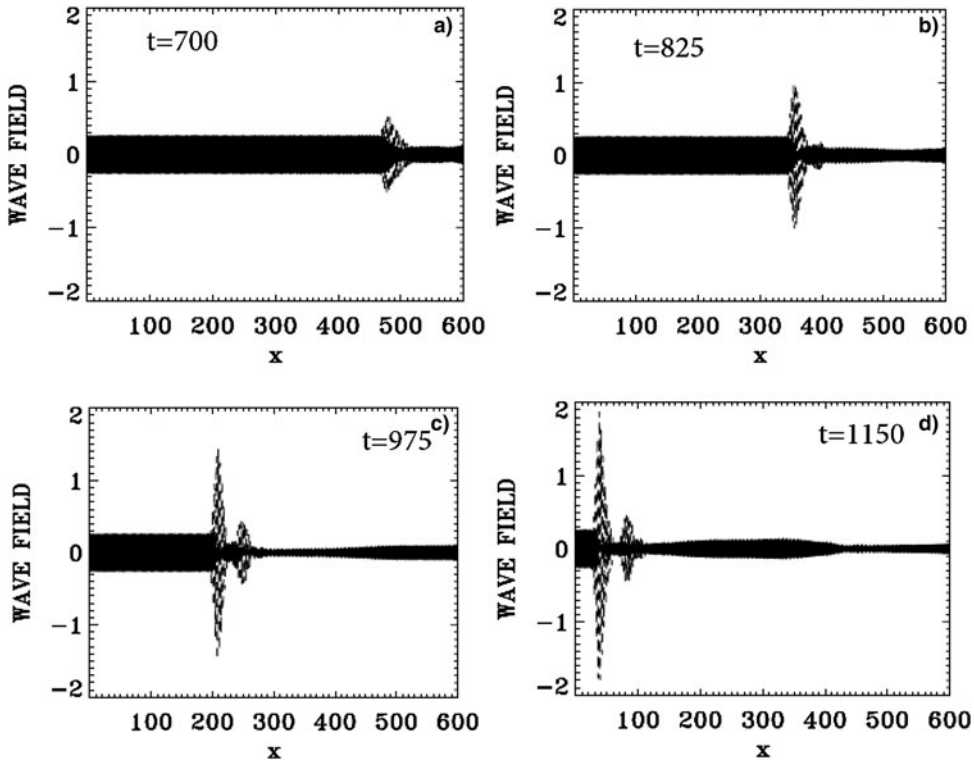

Fig. 16. The evolution of the incident pump wave E^+ (full curve) and the backward seed pulse E^- (dashed curve) at: (a) $t = 700$, (b) $t = 825$, (c) $t = 975$, (d) $t = 1150$.

value of 2.07 calculated in Figure 14]. From the plasma wave dispersion relation $\omega_e^2 = 1 + 3k_e^2(\upsilon_t^2/c^2)$, and T_e is 0.35 keV in the present calculation, we get for $k_e = 1.0$ the plasma frequency $\omega_e = 1.00$, which is the result we see in Figure 15 in the frequency spectrum of the longitudinal electric field.

The evolution of the incident pump wave E^+ (full curve) and the backward seed pulse E^- (dashed curve) are shown in Figure 16 at: (a) $t = 700$, (b) $t = 825$, (c) $t = 975$, (d) $t = 1150$. We note the growth and compression of the seed pulse E^-, propagating toward the left, together with an increase in the waveform steepness. The modulation we see behind the front pulse of the growing seed are due to the fact that when the pump depletes, the seed pulse will act as a source for the pump, which results in a modulation behind the growing seed. The constant amplitude full-curve at the left in Figure 16 is for the injected constant amplitude pump. At $t = 1150$, the backward seed pulse is about 25 times its original amplitude, and about eight times higher than the pump amplitude.

In what we present next, we will follow at different time the growth of the backward propagating seed pulse in different sections of the domain. In the results we analyze, we will show the dominance of a backward Raman scattering in the process of the amplification of the backward seed pulse all over the domain.

We present in Figure 17 the wavenumber spectra at the time $t = 720$ in the same domain $x = (450, 532)$ as in Figure 14, that is, after the arrival in this domain of the seed pulse injected with $\omega_{0S} = 2.17$ from the right boundary. In Figure 17, we see a dominant wavenumber for the backward wave E^- at $k_{0S} = 2.07$. The corresponding frequency spectra are given in Figure 18, calculated by taking a temporal Fourier transform in the time interval $t = (685,767)$, by monitoring the signal at the position $x = 450$. We see for the backward wave E^- a dominant broad peak at $\omega_{0S} = 2.147$, very close to the injected value of 2.17. The corresponding wavenumber to the frequency 2.147 calculated from the dispersion relation in Eq. (7) is 2.00, very close to the value of 2.07 calculated for the wavenumber of E^- in Figure 17. We see the trace of the backward mode at 2.07 in the spectrum of E^- appearing in the spectrum of E^+ in Figure 17 at 2.07, together with the wavenumber of the forward propagating pump wave E^+ at $k_{0P} = 3.068$. The corresponding frequency of the forward pump E^+ in Figure 18 is $\omega_{0P} = 3.22$.

The plasma wavenumber k_e and frequency ω_e must satisfy the selection rule for the momentum and energy conservation relations for the backward wave $k_{0P} = -k_{0S} + k_e$, and $\omega_{0P} = \omega_{0S} + \omega_e$. We get $\omega_e = 1.07$, and $k_e = 5.138$, which is the peak value we see in Figure 17 for the spectrum of the electric field, which shows the value of 5.138 and its harmonics. From the plasma wave dispersion relation $\omega_e^2 = 1 + 3k_e^2(\upsilon_t^2/c^2)$, we get for the plasma frequency $\omega_e = 1.0267$ for $T_e = 0.35$ keV, with the value $k_e = 5.138$, close to the value of 1.07

https://doi.org/10.1017/S0263034616000185 Published online by Cambridge University Press

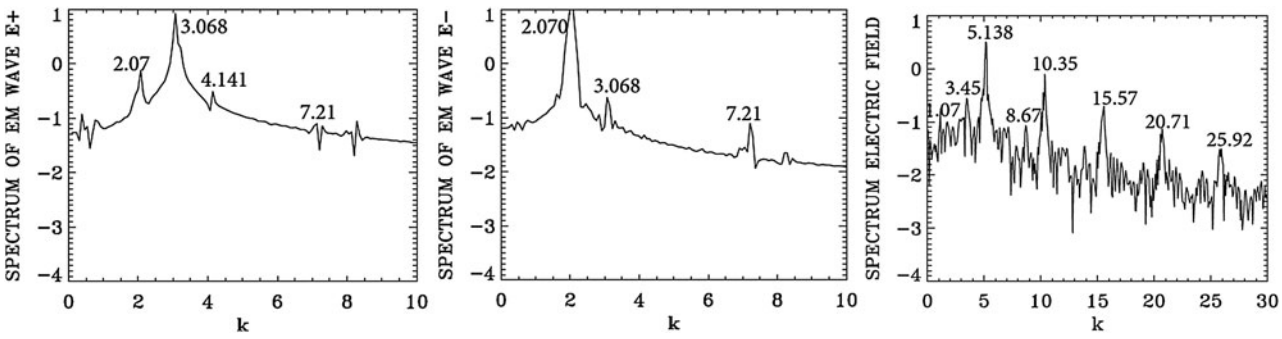

Fig. 17. Spatial Fourier transform of the incident pump wave E^+, the backward wave E^-, and the longitudinal electric field E_x, calculated in the domain $x = (450,532)$ at time $t = 720$.

calculated from the selection rule. We note a broad spectrum around 1.0 in Figure 18 for the plasma wave frequency. Note also the harmonic structure associated with the plasma frequency.

We note also in Figure 17 the plasma wave at 1.07 and the pump wave at the wavenumber 3.068 will combine to excite the anti-Stokes at 4.138, close to the value of 4.141 we see in the spectrum of E^+ in Figure 17. The corresponding frequencies in Figure 18 of 1.00 and 3.22, excite the anti-Stokes at the frequency 4.22 (a very small bump, not marked in the frequency spectrum of E^+ in Figure 18). The corresponding wavenumber to the frequency 4.22 calculated from Eq. (7) for the LCP wave is 4.12, very close to the value of 4.141 in Figure 17.

In addition to the backward scattering $k_{0P} = -k_{0S} + k_e$, $\omega_{0P} = \omega_{0S} + \omega_e$, which is exciting the backscattered mode in E^- at $\omega_{0S} = 2.147$ (see Figure 18) and $k_{0S} = 2.07$ (see Figure 17) we have a weak forward scattered mode at the same wavenumber and frequency $k_{0P} = k_{0S} + k_e$, from which $k_e = 3.068 - 2.07 = 0.997$ (close to the value of 1.07 we see in Figure 17), and $\omega_e = \omega_{0P} - \omega_{0S} = 3.22 - 2.147 = 1.073$ (see the broad peak around 1.0 in Figure 18).

We follow again the backward Raman scattering amplification in another domain closer to the left boundary. We present in Figure 19 the wavenumber spectra close to the left boundary, in the domain $x = (30, 112)$ at $t = 900$, before the arrival of the injected backward seed pulse which, at $t = 900$, has only reached around the point $x = 240$. The spectrum for the pump E^+ shows a dominant peak of the forward pump at $k_{0P} = 3.068$. As we mentioned above, E^+ and E^- are strictly decoupled in vacuum, a very small backward wave E^- at the same wavenumber 3.068 results from the coupling with E^+ in the nonlinear plasma medium; otherwise no other backward or forward scattered wave is present, before the arrival of the backward seed pulse.

We present in Figure 20 the frequency spectrum corresponding to the results presented in Figure 19, calculated by monitoring the signal at the position $x = 80$, and making a temporal Fourier transform of the signal in the interval of time $t = (500,582)$, before the arrival of the backward seed pulse. The peak frequency of the injected pump E^+ at 3.2 is appearing in Figure 20 at 3.22. So only the forward pump is present before the arrival of the backward signal. Again, as explained before, there is a small backward wave E^- at the same frequency, which results from the coupling in the nonlinear plasma medium with E^+, but no other backward or forward scattered wave is present before the arrival of the counter-propagating backward seed pulse.

In Figure 21, we present a plot for the electron density profile at $t = 975$ (left frame). The right frame in Figure 21 zoom on the front edge of the profile, in $x \in (200, 250)$, which shows clearly the regular oscillations of the dominant growing mode with wavenumber $k_e = 5.138$, and wavelength

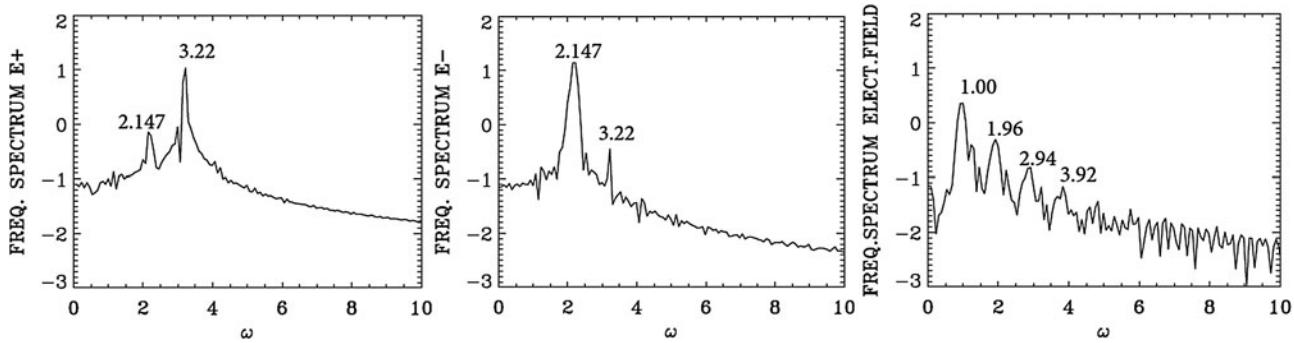

Fig. 18. Temporal Fourier transform of the incident pump wave E^+, the backward wave E^-, monitored at the position $x = 450$, in the time interval $t = (685,767)$.

https://doi.org/10.1017/S0263034616000185 Published online by Cambridge University Press

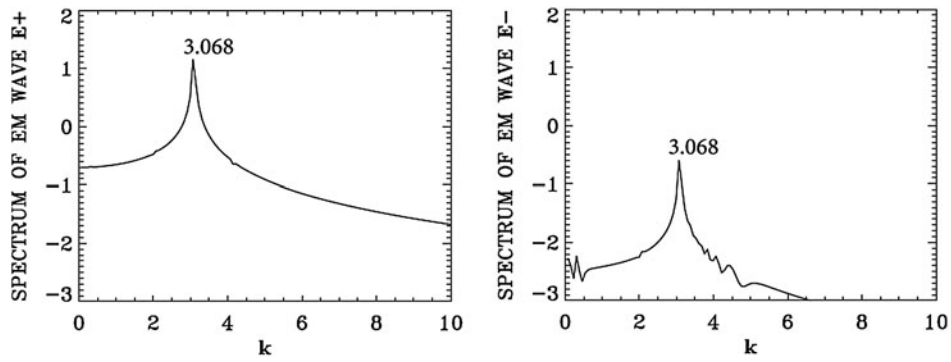

Fig. 19. Spatial Fourier transform of the incident pump wave E^+, the backward wave E^-, in the domain $x = (30,112)$ at $t = 900$.

$\lambda_e = 2\pi/k_e = 1.22$. Figure 22 presents a plot for the electron density profile at $t = 1150$ (left frame). The right frame in Figure 22 zoom on the front edge of the profile, in $x \in (30, 80)$. Figure 24 below shows the dominant mode at that time has shifted to $k_e = 5.292$, with the corresponding wavelength $\lambda_e = 2\pi/k_e = 1.18$. So the growth of the pulse is continuing, as verified from Figure 16, as long as the front part of the pulse is maintaining its coherent structure. In the domain besides the front part, the fusion of the vortices in phase-space due to the competing modes creates a chaotic structure (see Figure 25 below).

We present in Figure 23 the frequency spectrum at the front part of the growing pulse, by monitoring the signal at the position $x = 80$, calculated by taking the temporal Fourier transform in time in the interval $t = (1100,1192)$ after the arrival of the backward signal. Figure 16 shows the steepening of the profile. We see again the peak frequency of the forward pump E^+ at 3.2 is appearing in Figure 23 at 3.22. The

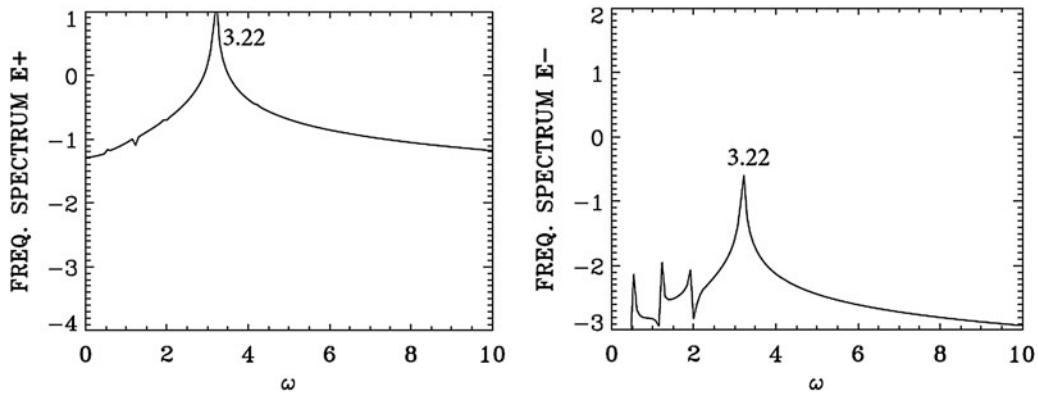

Fig. 20. Temporal Fourier spectrum of the incident pump wave E^+, the backward wave E^-, monitored at the position $x = 80$, in the time interval $t = (500,582)$.

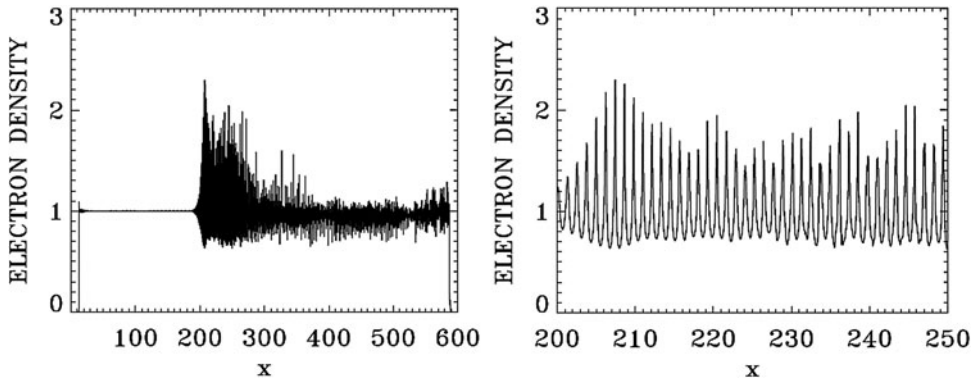

Fig. 21. Plot of the electron density profile at $t = 975$.

https://doi.org/10.1017/S0263034616000185 Published online by Cambridge University Press

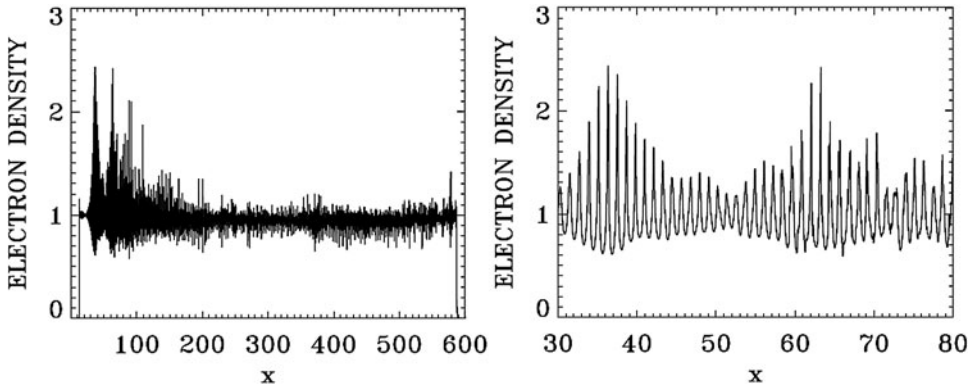

Fig. 22. Plot of the electron density profile at $t = 1150$.

backward wave E^- shows now dominant frequencies over a broad peak extending from 2.147 to 2.301 (the backward seed was injected at the right boundary at the frequency 2.17). This same frequencies (2.147, 2.301) are appearing in the spectrum of E^+ due the coupling in the nonlinear plasma medium. The backward seed pulse arrived at the position $x = 80$ at about $t = 1120$. So the frequency spectrum of the electric field is still at its early development and did not have the time to develop a harmonic structure as in Figure 18. It shows a broad peak around 1.0.

We present in Figure 24 the wavenumber spectra at the front part of the growing pulse, by taking the spatial Fourier transform in the domain $x = (30, 112)$ at $t = 1150$. Slightly broader peaks are appearing in the wavenumber spectrum for E^- at 1.994 and 2.147 corresponds to the frequencies for E^- at 2.147 and 2.30, respectively in Figure 23 [from Eq. (7), for a LCP wave, for a frequency 2.147 corresponds a wavenumber 2.00, and for a frequency 2.30 corresponds a wavenumber 2.16, very close to the peak values of 1.994 and 2.147 we see in Figure 24 for E^-]. For E^+, we have in

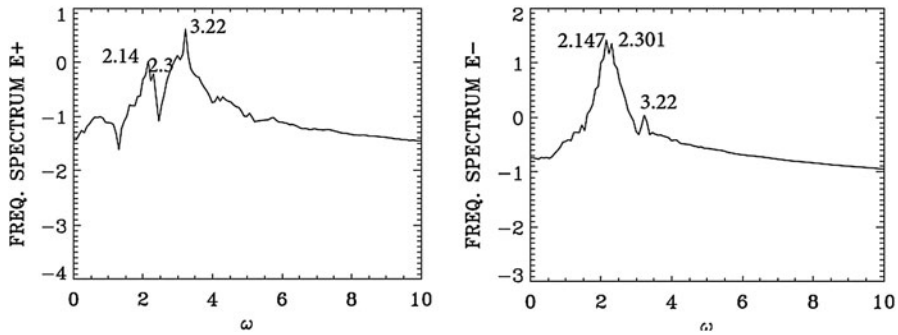

Fig. 23. Temporal Fourier transform for the incident pump wave E^+, and the backward wave E^-, monitored at the position $x = 80$, in the time interval $t = (1100,1192)$.

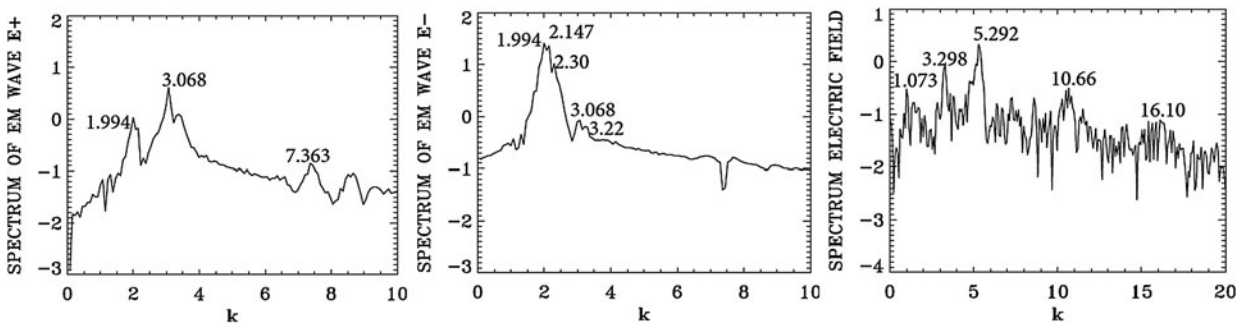

Fig. 24. Spatial Fourier transform of the forward wave E^+, the backward wave E^- and the longitudinal electric field E_x, in the domain $x = (30,112)$ at $t = 1150$.

https://doi.org/10.1017/S0263034616000185 Published online by Cambridge University Press

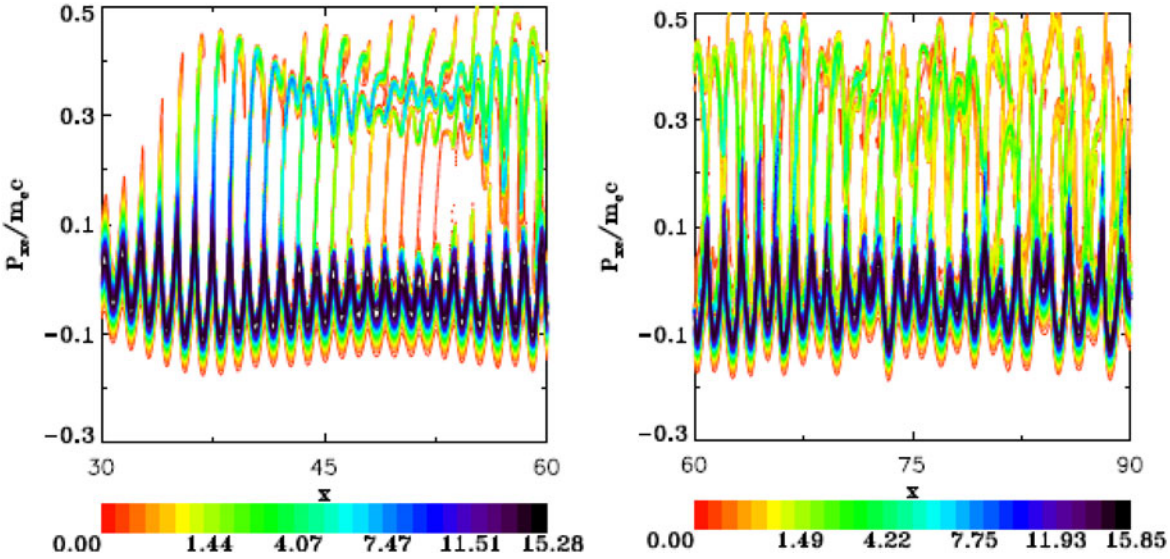

Fig. 25. Contour plot of the electron distribution function at $t = 1150$, for $30 < x < 60$ and $60 < x < 90$.

Figure 24 the wavenumber 3.068, corresponding to the frequency 3.22 in Figure 23 (the injected pump frequency for E^+ is 3.2 as previously mentioned).

The plasma wavenumber k_e and ω_e must satisfy the selection rule for the momentum and energy conservation relations for the backward wave $k_{0P} = -k_{0S} + k_e$, and $\omega_{0P} = \omega_{0S} + \omega_e$. With $k_{0P} = 3.068$ and $k_{0S} = 2.147$ we get $k_e = 5.215$, which is very close to the value we see in Figure 24 for the spectrum of the electric field E_x which shows the peak at 5.292 and its harmonics. From the plasma wave dispersion relation $\omega_e^2 = 1 + 3k_e^2(v_t^2/c^2)$, we get for the plasma frequency $\omega_e = 1.028$ for $T_e = 0.35$ keV, with the value $k_e = 5.292$, close to the value of 1.07 calculated from the selection rule. Note in the spectrum of E^+ the presence of a weak forward coupling with the mode at the wavenumber 1.994, following the selection rule $3.068 = 1.994 + 1.074$ (see the plasma mode at 1.073 in Figure 24).

The left frame in Figure 25 shows the contour plot of the electron distribution function at $t = 1150$ at the front edge in $x \in (30, 60)$. It shows in the left frame the regular oscillations of the dominant growing mode of the steep pulse with the wavelength $\lambda_e = 2\pi/k_e = 1.18$, corresponding to dominant value of $k_e = 5.292$ we see in Figure 24. In the right frame, the phase-space contour plot of the distribution function at $t = 1150$ in $x \in (60, 90)$ shows a tendency to become more chaotic, as it is also apparent in the density plot of Figure 22.

In the results we have presented in this section, we have followed at different positions and time the growth of the backward propagating seed-pulse in different section of the domain. In the results we analyzed we have shown the dominance of a backward SRS in the process of the amplification of the backward seed-pulse all over the domain. We have also shown that before the arrival of the counter-propagating backward seed pulse, no backward SRS was present in the domain.

5. THE CASE OF THE BRILLOUIN AMPLIFICATION OF A SEED PULSE

We consider a plasma such that the electron cyclotron frequency is $\Omega_{ce} = 1.4$, and the laser pump frequency is $\omega_{0P} = 2.17$. From Eq. (7), the corresponding wavenumber for a LCP wave is 2.025, and for a RCP wave the corresponding wavenumber is 1.376. The SBS produces a very small frequency downshift in the scattered wave $\omega_{0P} = \omega_{0S} + \omega_{ion}$. We neglect this small downshift $\omega_{ion} \ll 1$ and set the seed frequency $\omega_{0S} \approx \omega_{0P} = 2.17$ for a LCP wave (and hence $k_{0S} \approx k_{0P} = 2.025$). The SBS is backward-propagating, so the selection rule is $k_{0P} = -k_{0S} + k_{ion}$, and hence the wavenumber of the ion wave $k_{ion} \approx 2k_{0P} = 4.05$. We also take for the vector potentials of the waves $a_{0S} = a_{0P} = 0.04$, and the parameters of the counter-propagating seed pulse injected at the right boundary are the same as in Eq. (8). We have the same length $L = 600$ as in the previous section.

For the electron distribution function, the extrema of momentum for the electrons are ± 0.5, and with 1000 grid points in velocity space, we have a grid size of $\Delta v = 10^{-3}$. For the ions the extrema of momentum are $\pm 1.46 \times 10^{-3}$, and with 500 grid points in velocity space, we have a grid size of $\Delta v = 5.85 \times 10^{-6}$. The initial distribution functions are Maxwellian with temperatures $T_e = 0.3$ keV for the electrons and $T_i = 0.02$ keV for the ions. The parameters of the plasma slab are the same as in Section 4, with $\Delta x = \Delta t = 0.005$.

We present in Figure 26 the wavenumber spectra in the domain $x = (30, 224)$ at $t = 600$, before the arrival of the injected backward seed-pulse, which at $t = 600$ has only penetrated to the point $x = 540$, according to the discussion for Eq. (8) of the previous section. The spectrum for the pump E^+ shows a dominant peak at $k_{0P} = 2.0325$, very close to

https://doi.org/10.1017/S0263034616000185 Published online by Cambridge University Press

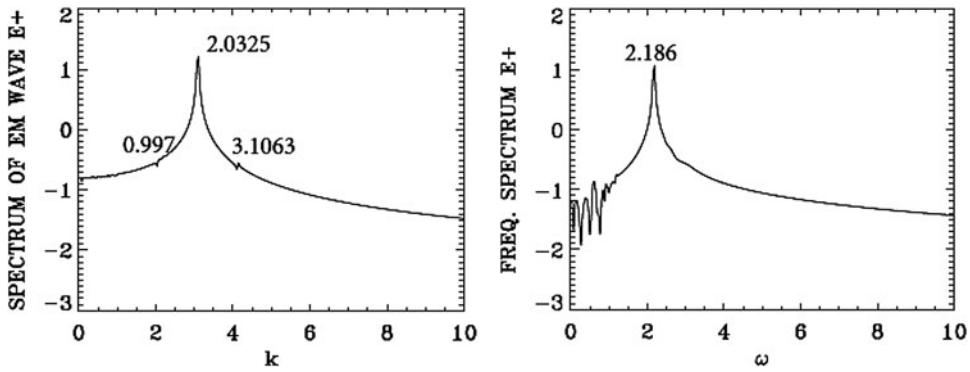

Fig. 26. Spatial Fourier spectrum of the incident pump wave E^+ in the domain $x = (30,224)$ at $t = 600$ (right frame), and temporal Fourier spectrum of the incident pump wave E^+ in the time interval $t = (100,294)$ at the position $x = 90$ (left frame).

the value of 2.025 calculated as mentioned above from Eq. (7) for the LCP wavenumber response to the injected pump at $\omega_{0P} = 2.17$. Figure 26 shows also for the frequency spectrum of the pump (in the right frame) the value of 2.186, very close to the injected value of 2.17. The frequency spectrum is calculated by taking the temporal Fourier transform of the signal, recorded at the position $x = 90$ in $t = (100,294)$. The forward pump is the only wave present, the backward seed pulse did not reach the domain $x = (30, 224)$ at $t = 600$. So the spectrum of E^- is essentially the same as in Figure 26, due to the coupling of E^- and E^+ in the nonlinear plasma medium, with E^- much smaller than E^+ as previously mentioned. There is no backward scattered mode. Figure 26 shows also a small forward excited wave at 0.997, satisfying $k_{0P} = 0.997 + k_{e1}$, from which we have for the plasma wave of the longitudinal electric field $k_{e1} = 2.0325 - 0.997 = 1.0355$, and the corresponding frequency calculated from the plasma wave dispersion relation $\omega_{e1}^2 = 1 + 3k_{e1}^2(v_t^2/c^2)$, from which $\omega_{e1} = 1.00$. The spatial spectrum of the longitudinal electric field shows indeed a small peak at 1.0738, and the temporal spectrum shows indeed a peak at 1.00. This will be discussed in more details in Figures 28 and 29. In Figure 26, we have also a very small trace of the anti-Stokes at 3.1063, resonating with a plasma wave at the wavenumber 1.0738 = 3.1063–2.0325, with a corresponding plasma frequency of 1.00. The frequency resonance is $2.186 + 1.00 = 3.186$. The wavenumber for the anti-Stokes calculated from Eq. (7) for the frequency 3.186 is 3.075, close to the value of 3.1063 in Figure 26. There is no backward seed pulse injected at the right boundary which has yet arrived in the domain $x = (30, 224)$.

The evolution of the incident pump wave E^+ (full curve) and the backward seed pulse E^- (dashed curve) are shown in Figure 27 at: (a) $t = 1000$, (b) $t = 1225$. We note the growth and contraction of the seed pulse, propagating toward the left. The modulation we see behind the front pulse of the growing seed are due to the fact that when the pump depletes, the seed pulse will act as a source for the pump, which results in a modulation behind the growing seed. The constant amplitude full-curve at the left in Figure 27(a) is for the constant amplitude incident pump. The original amplitude of the seed was equal the amplitude of the pump. At the end at $t = 1225$ in Figure 27, the backward seed pulse is about two times of its original amplitude.

In Figure 28, the wavenumber spectra associated with the forward wave E^+, the backward wave E^-, the longitudinal electric field E_x, and the ion density, are calculated by Fourier transform of the corresponding signal in the domain $x = (200,394)$, which has been reached by the backward seed pulse at $t = 1000$. The spectrum of the electron density is essentially the same as the one presented for the longitudinal electric field in Figure 28. The spectrum of E^+ in Figure 28

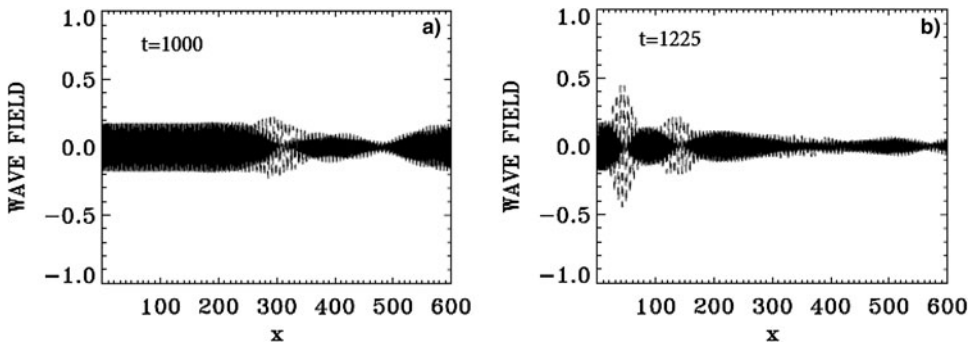

Fig. 27. The evolution of the incident pump wave E^+ (full curve) and the backward seed pulse E^- (dashed curve) at: (a) $t = 1000$, (b) $t = 1125$.

https://doi.org/10.1017/S0263034616000185 Published online by Cambridge University Press

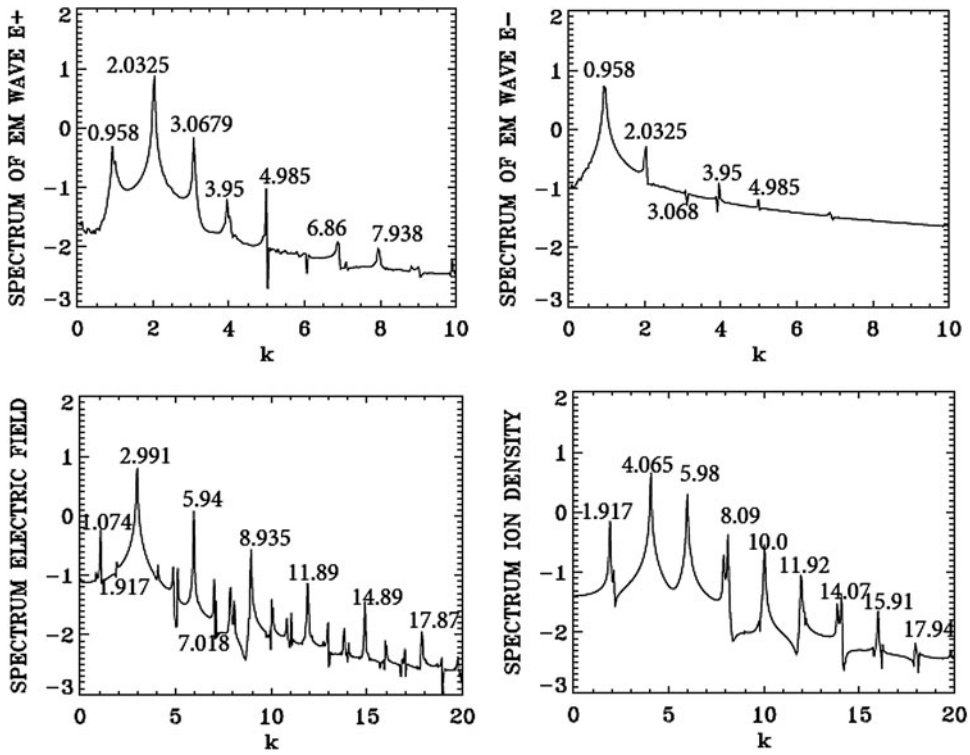

Fig. 28. Spatial Fourier transform of the forward pump wave E^+, the backward seed pulse E^-, the longitudinal electric field E_x and the ion density in the domain $x = (200,394)$ at $t = 1000$.

shows the peak of the forward pump at 2.0325, as we mentioned in Figure 26, and the same mode appearing as a backward mode in the spectrum of E^- in Figure 28. The presence of these two modes will result in the appearance of a backward Brillouin scattering as discussed above, with an ion wavenumber $k_{\rm ion} \approx 2k_{0\rm P} = 4.065$, which is indeed appearing the spectrum of the ion density in Figure 28. We also note in the spectrum of E^+ in Figures 26 and 28 the presence of the forward scattered mode at 0.958, with the plasma mode at 1.074 apparent in the spectrum of the electric field E_x in Figure 28, such that 2.032 = 0.958 + 1.074. The corresponding frequencies we see in Figure 29, calculated by taking the temporal Fourier transform of the signal recorded at $x = 300$, between $t = (1000,1194)$, give a frequency $\omega_{0\rm P} = 2.186$ for the pump and $\omega_{0\rm S} = 1.186$ for the forward scattered mode. The corresponding wavenumbers calculated from Eq. (7) are respectively 2.042 (very close to the value of 2.032 in Figure 28) and 0.973 (very close to the value of 0.958 in Figure 28). This gives a plasma wavenumber 1.069 = 2.042–0.973, close to the value of 1.074 calculated in Figure 28 in the spectrum of E_x. The corresponding plasma frequency is calculated from the plasma wave dispersion relation $\omega_{\rm e}^2 = 1 + 3k_{\rm e}^2(\upsilon_{\rm t}^2/c^2)$. We get for $k_{\rm e} = 1.069$ the plasma frequency $\omega_{\rm e} = 1.00$, in good agreement with the value in Figure 29 in the spectrum of E_x, satisfying the frequency selection rule 2.186–1.186 = 1.00.

We have also in the spectrum of E^- a backward scattered mode at 0.985 in Figure 28, which is dominating the

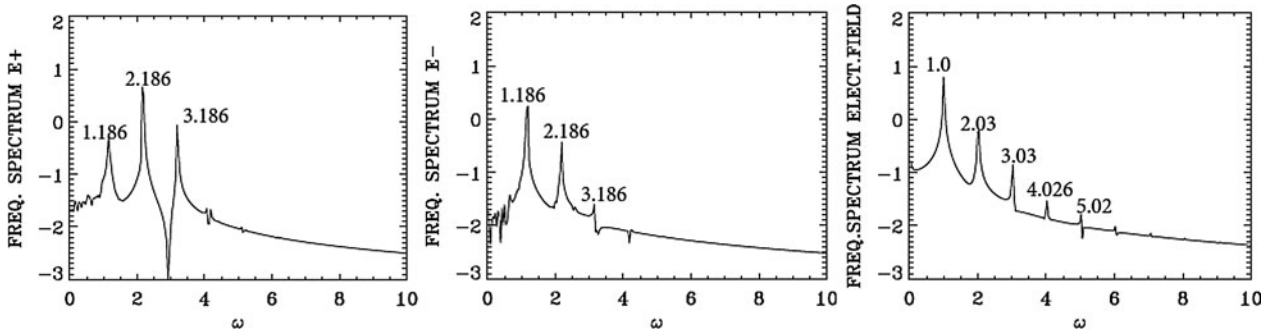

Fig. 29. Temporal Fourier transform of the signal recorded at $x = 300$, in the time interval $t = (1000,1194)$, for the forward pump wave E^+, the backward wave E^-, and the longitudinal electric field E_x.

https://doi.org/10.1017/S0263034616000185 Published online by Cambridge University Press

spectrum of E^-, such that $k_{0P} = -k_{0S} + k_e$, that is $2.0325 = -0.985 + 2.9905$. We see indeed the mode at 2.991 in the spectrum of the electric field in Figure 28. The forward scattered mode at 0.985 in E^+ and the backward mode in E^- at 0.985, will couple through Brillouin scattering to give another Brillouin scattered mode at $k_{ion} \approx 2 \times 0.958 = 1.916$, which appears at 1.917 in the spectrum of the ion density in Figure 28. So we have two Brillouin scattering events, one at $k_{ion} \approx 2k_{0P} = 4.065$ through direct scattering from the pump E^+ and the backward seed pulse, and the second one through an intermediate step of forward and backward Raman scattering of the pump, which produced the modes at 0.958 in E^+ and -0.958 in E^-, from which the ion mode wavenumber $\approx 2 \times 0.958 = 1.916$. Other resonances are also present. We can identify in the spectrum of E^+ the anti-Stokes at 3.0679 obtained by the coupling of the plasma mode at 1.074 and the pump E^+ at the wavenumber at 2.0325 such that $3.1065 = 2.0325 + 1.074$, close to the value of 3.0679 we see in the wavenumber spectrum of E^+ in Figure 28. From Figure 29 the corresponding longitudinal plasma frequency is $\omega_e = 1.00$, the corresponding frequency to the anti-Stokes mode is 3.186, which verifies the selection rule for the frequencies $3.186 = 2.186 + 1.00$. The wavenumber for the anti-Stokes calculated from Eq. (7) for the frequency 3.186 is 3.075, close to the value of 3.0679 in Figure 28.

The modes in E^+ in Figure 28 at 2.035 and 3.95 will combine with the mode at 1.917 in the longitudinal electric field such that $3.95 = 2.0325 + 1.917$, with the corresponding frequencies in Figure 29 satisfying the selection rule $3.18 + 1.01 = 4.19$ (the unmarked small peak in Figure 29 in the spectrum of E^+).

The forward mode at 4.985 in E^+ and the backward mode at -0.985 in E^- in Figure 28 will couple to produce the mode in the longitudinal electric field $4.985 = -0.985 + k_e$, from which the plasma wavenumber $k_e = 5.94$, which appears in the spectrum of E_x in Figure 28. The ion mode at 5.98 will couple with the two ion modes at 4.065 and 1.915, $4.065 + 1.915 = 5.98$, and the ion mode at ten couples with two ion modes $4.065 + 5.98 = 10.045$, and with the two ion modes $8.09 + 1.917 = 10.007$. The corresponding ion acoustic frequencies for these ion modes with the dispersion relation $\omega = kC_s$, where C_s is the ion acoustic speed, will automatically satisfy the selection rules, because of the linear dependence of ω and k in the dispersion relation of the ion acoustic waves.

We note the harmonic structure associated with the plasma wavenumber of 2.991 in the wavenumber spectrum of the longitudinal electric field in Figure 28 at 5.94, 8.935, 11.89, 14.89, 17.87, and the harmonic structure with the plasma frequency in Figure 29. We also note the harmonic structure associated with the ion mode at the wavenumber 4.065 at 8.09, 11.92, 15.91, and the harmonic structure associated with the ion mode with the wavenumber 5.98 at 11.92 and 17.94 in Figure 28.

Figure 30 presents a plot for the electron density profiles at $t = 900$, 1000, and 1225. Similar plots are presented in Figure 31 for the ion density profiles, and in Figure 32 for the electric field profiles. In Figure 33, we zoom on the front edge of the profiles in $x = (30, 80)$, which shows at $t = 1225$ the regular oscillations of the dominant growing mode with wavelength $\lambda_e = 2\pi/2.99 = 2.1$ for the electron density and the longitudinal electric field, and $\lambda_i = 2\pi/4.065 = 1.54$ for the ion density profile (Figs 33–35).

In the results, we have presented in this section, two backward Brillouin scattering events are present. The first one results directly from the pump and the counter-propagating seed pulse, both injected at the same frequency $\omega_{0S} \approx \omega_{0P} = 2.17$. The second backward Brillouin scattering event takes place via the intermediate step of two Raman scattering processes, which create the counter-propagating modes in E^+ and E^- at the wavenumber 0.958, and a resulting SBS mode at the wavenumber $2 \times 0.958 = 1.916$, which we see in Figure 28 in the spectrum of the ion density.

6. THE CASE OF THE WAKEFIELD ACCELERATOR IN A MAGNETIZED PLASMA

A solution of this problem in an un-magnetized plasma using an Eulerian Vlasov code has been given by Shoucri (2008*b*). The application of an external magnetic field in the problem of wakefield acceleration has been suggested by Grulke *et al.* (2015) to stabilize the plasma column. We consider a plasma such that the ratio of the electron cyclotron frequency to the

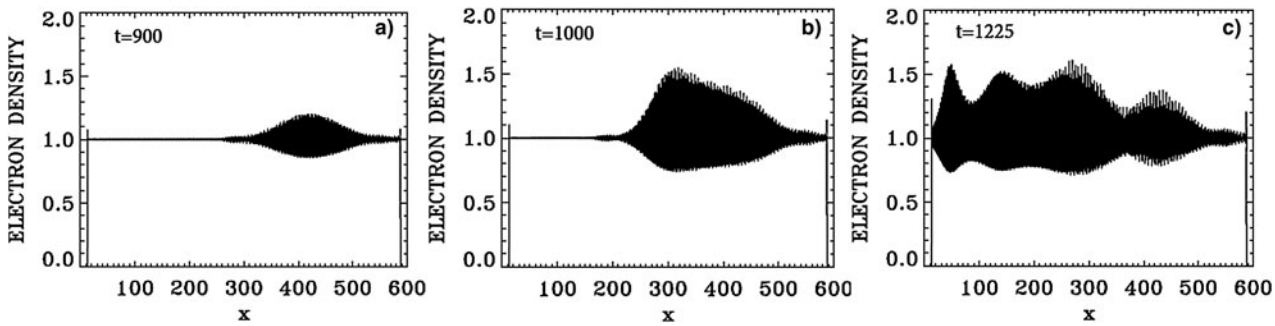

Fig. 30. Plot of the electron density profiles at: (a) $t = 900$, (b) $t = 1000$, (c) $t = 1225$.

https://doi.org/10.1017/S0263034616000185 Published online by Cambridge University Press

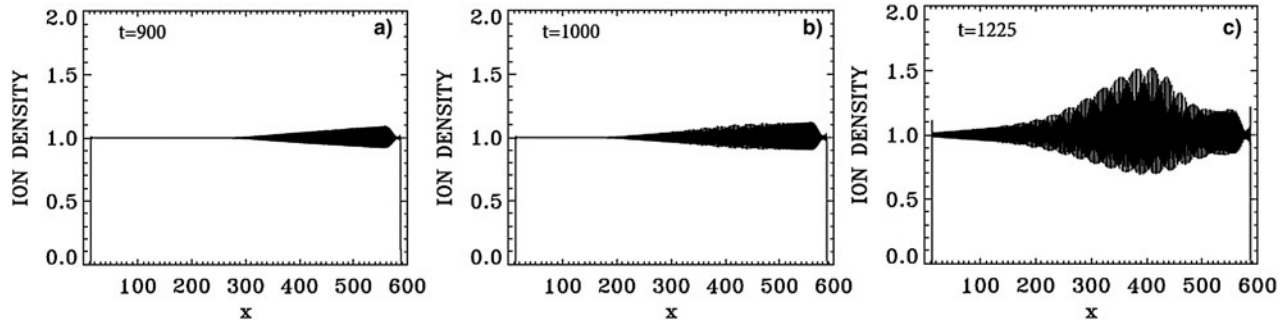

Fig. 31. Plot of the ion density profiles at: (a) $t = 900$, (b) $t = 1000$, (c) $t = 1225$.

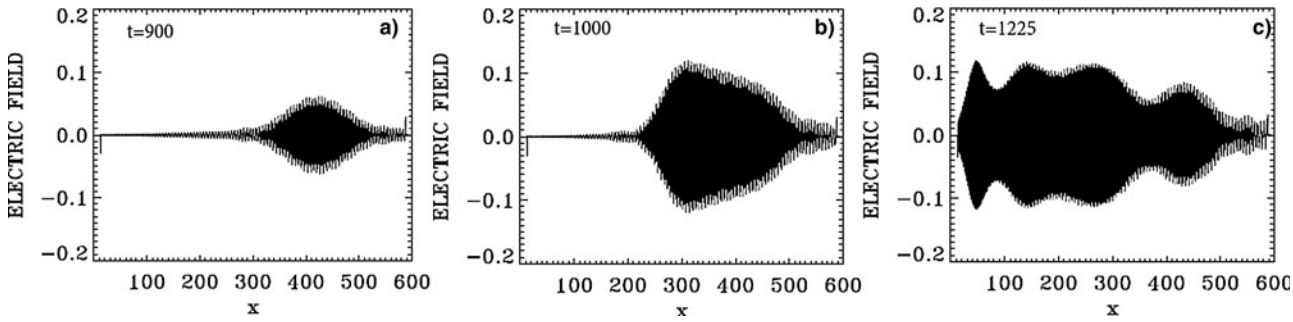

Fig. 32. Plot of the longitudinal electric field E_x at: (a) $t = 900$, (b) $t = 1000$, (c) $t = 1225$.

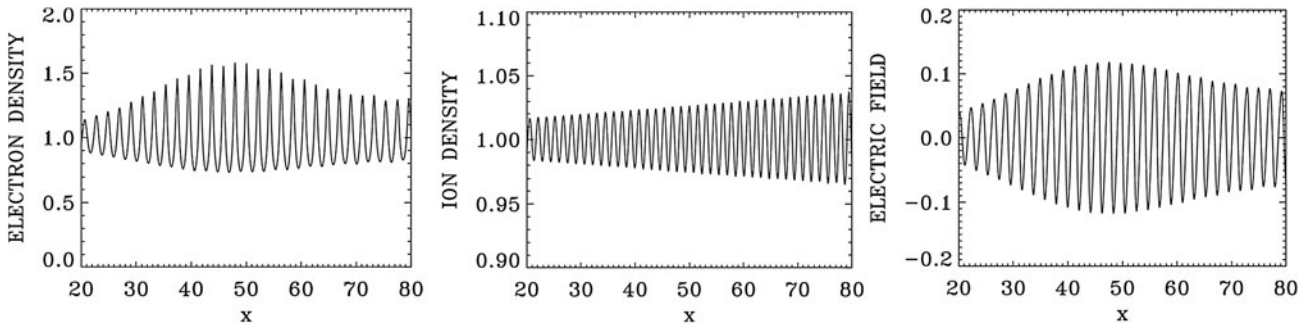

Fig. 33. Zoom on the front edge of the profiles in $x = (30,80)$ at $t = 1225$.

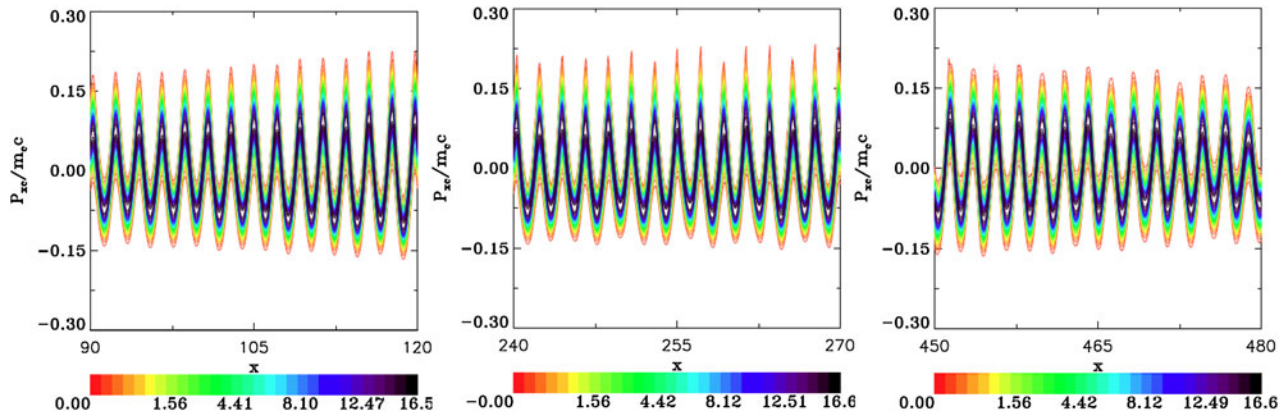

Fig. 34. Phase-space contour plot of the electron distribution function at $t = 1225$, at different positions.

https://doi.org/10.1017/S0263034616000185 Published online by Cambridge University Press

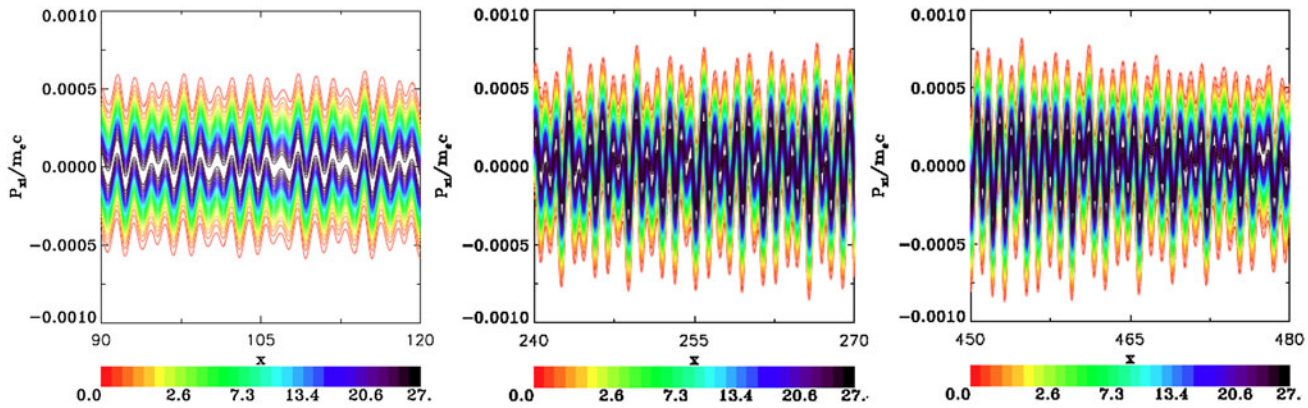

Fig. 35. Phase-space contour plot of the ion distribution function at $t = 1225$, at different positions.

electron plasma frequency $\Omega_{ce} = 0.1$, and the ratio of the laser pump frequency to the electron plasma frequency $\omega_{0P} = 10 \gg 1$. We use $N_x = 50\,000$ grid points in space for a total length of the plasma $L = 50$. The extrema of the electrons momentum are ± 20, with a number of grid points $N_{pe} = 5000$, and for the ions momentum extrema we have $\pm 1.25 \times 10^{-4}$, with a number of grid points $N_{pi} = 400$. The electron and ion temperatures are $T_e = 0.2$ keV and $T_i = 0.01$ keV. The length of the vacuum region is 0.166 on each side, and the length of the transition region for the zero density to the flat density of 1 is 1.0 on each side of the slab, hence a total transition region of 1.166 on each side of the plasma slab. The system is initially neutral ($n_e = n_i$), with the density in the flat neutral part equal to 1 in our normalized units. We note the ions density remained equal to 1 in the flat central part, the ions however showing a modulation in the phase-space contour plots.

The forward propagating circularly polarized laser pulse is penetrating from the vacuum at the left boundary at $x = 0$, and propagate toward the right, and is written in our normalized units as:

$$E^+ = 2E_0 \sin(\pi\xi/L_x)\sin(k_{0P}\xi), \tag{9}$$

$$F^- = 2E_0 \sin(\pi\xi/L_x)cos(k_{0P}\xi), \tag{10}$$

for $1 < t < 2\pi + 1$, and for $-L_x < \xi < 0$, $\xi = x - t$, and $E_0 = 0$ otherwise. The time delay 1 corresponds approximately to the length 1.166 of the vacuum and transition region as mentioned above. This allows the pulse to develop close to the edge of the flat part of the density profile. L_x is the length of the pulse envelope. In vacuum, we have for the EM wave $k_{0P} = \omega_{0P}$. So in our normalized units the vacuum wavelength $\lambda = 2\pi/k_{0P} = 0.628$. We have ten oscillations for the EM wave in the length $L_x = 2\pi$ of the pulse envelope. Note that the wavenumber inside the plasma can be calculated from Eq. (7), and for $\Omega_{ce} = 0.1$ and $\omega_{0P} = 10$ gives $k_{0P} \approx 9.95$, close to the vacuum value of 10. We choose for the amplitude of the potential vector $a_{0P} = 0.8$, so that $E_0 = \omega_{0P}a_{0P} = 8$. From Eqs. (9) and (10) the amplitude of E^+ and F^- are equal to $2E_0$. Since the envelope is very slowly varying, we can write for the corresponding vector potential for $1 < t < 2\pi + 1$:

$$a_y = -a_{0P} \sin(\pi\xi/L_x)cos(k_{0P}\xi), \tag{11}$$

$$a_z = a_{0P} \sin(\pi\xi/L_x)cos(k_{0P}\xi), \tag{12}$$

At $t = 2\pi + 1$, most of the entire envelope of length $\approx 2\pi$ of the forward propagating pulse has developed on the flat density part and is left to evolve self-consistently according to Eq. (5). Figure 36 shows the results for the laser pulse at $t = 50$ (broken curve, divided by 5 to allow visibility for the longitudinal electric field E_x), after crossing the domain and reaching the right boundary. It is followed by the wakefield E_x (full curve). There is little deformation of the EM pulse for the present set of parameters. Figure 37 shows the plot of the electron density (full curve), and the ion density (dashed curve). The modulation of the electron density is

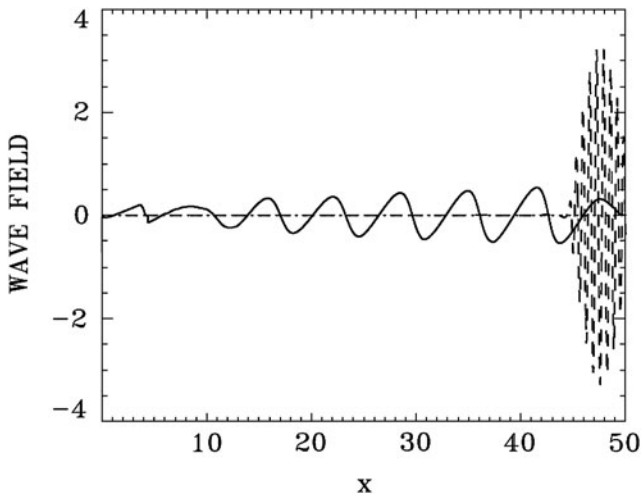

Fig. 36. Laser pulse $E^+/5$ at $t = 51$ (broken curve, divided by 5 to allow visibility for the longitudinal electric field E_x), after crossing the domain and reaching the right boundary. It is followed by the wakefield E_x (full curve).

https://doi.org/10.1017/S0263034616000185 Published online by Cambridge University Press

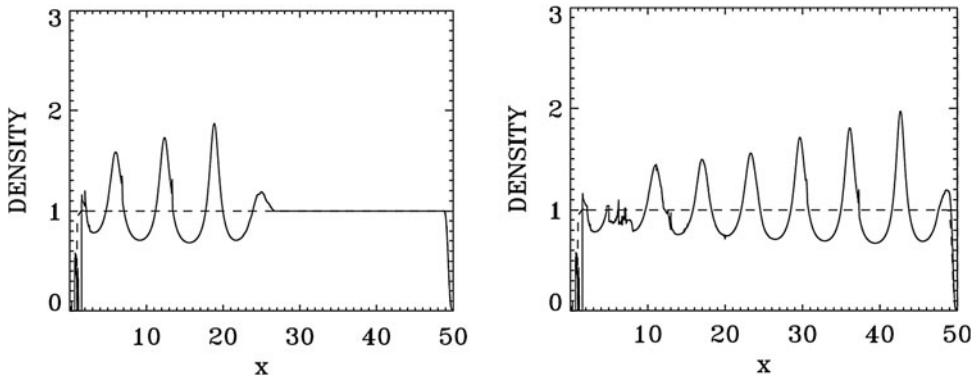

Fig. 37. Plot of the electron density (full curve) and the ion density (dashed curve) at $t = 27$ (left frame) and $t = 51$ (right frame).

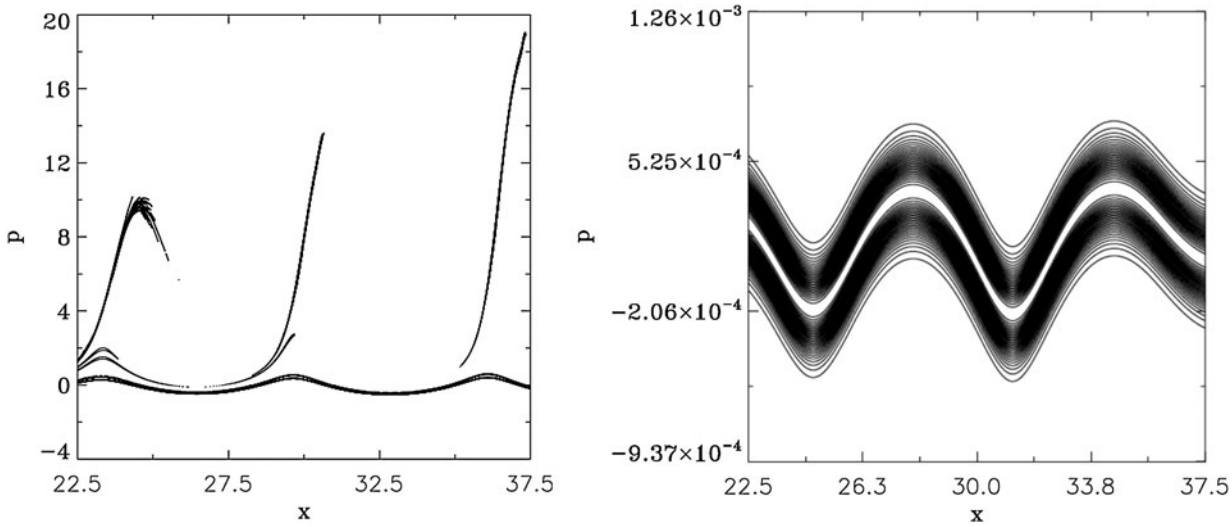

Fig. 38. Phase-space contour plot in $x = (22.5,37.5)$ of the electron distribution function (left frame) and the ion distribution function (right frame) at $t = 51$.

following the modulation of the wakefield in Figure 36. The ion density remains constant (if we accept a small deformation at the left of the domain due to the formation of a local sheath at the left edge). The longitudinal electric field E_x reaches in Figure 36 a peak of about 0.6.

Figure 38 shows the phase-space plots for the electrons (left frame) and the ions (right frame) at $t = 51$, in the domain $22.5 < x < 37.5$. Bunches of electrons detach from the bulk and are accelerated as beams around the peaks of the electric field (note that the contour levels of these accelerated beams are artificially enhanced in Figures 38 (left frame), in order to make them more visible). The ions density remained equal to 1 as mentioned in Figure 37, but are showing a modulation in phase space in Figure 38 (right frame), which follows the modulation of the electrons in Figure 38 (left frame).

7. CONCLUSION

Plasma-based laser amplifiers have received considerable attention for their application to the direct amplification of ultra-short laser pulses. A plasma-based amplifier approach benefits from the fact that a plasma can sustain much higher intensities than a solid-state amplifier. Most of the work being investigated by several groups in the study of these novel techniques for amplifying laser light to ever higher intensities has been essentially carried out in unmagnetized plasmas (see the references presented in the Introduction). In the present work, we have extended the study of plasma-based amplifiers to the case of magnetized plasmas. It has recently been suggested that the addition of a magnetic field can improve the plasma confinement and performance, as suggested for instance by Grulke *et al.* (2015), for problems of wakefield accelerators. This problem can also have important applications to understand the nonlinear growth of waves in the magnetosphere and other geophysical situations (see the review article by Briand, 2015), and in many other situations where a magnetic field is imposed on the plasma, as recently studied for the case of a magnetic field imposed in inertial confinement fusion indirect-drive hohlraum plasmas (Montgomery *et al.*, 2015; Strozzi *et al.*, 2015).

https://doi.org/10.1017/S0263034616000185 Published online by Cambridge University Press

We have presented in the present work an Eulerian Vlasov code to study the problem of the one-dimensional (1D) plasma-based seed-pulse amplifier for a plasma in a magnetic field. The code has been previously applied to study for instance the problem of beat-wave acceleration for a plasma in a magnetic field (Ghizzo *et al.*, 1992). The numerical simulations we present in Sections 4 and 5 on the application of backward SRS and SBS for seed-pulse amplification when a magnetic field is applied to the plasma are, to our knowledge, the firsts on this subject. The code applies a method of fractional step (Shoucri & Storey, 1986; Ghizzo *et al.*, 1990, 1992; Shoucri, 2008*a*) for the solution of the 1D relativistic Vlasov–Maxwell set of equations for a plasma in a magnetic field. We have first tested the performance of the code by studying its performance and response in Section 3 to a large amplitude laser wave. For the application to the problem of plasma amplifiers presented in Sections 4 and 5, we have studied the energy transfer through scattering mediated by a resonant plasma wave, for a long pump EM wave, to an initially counter-propagating short seed pulse. In Section 4, the resonant plasma wave is an electron plasma wave in a case of backward SRS. We have followed in this case the amplification of the backward seed pulse at different positions and different times, and we have shown that the backward SRS was the dominant mechanism in the amplification process. In Section 5, the resonant plasma wave is an ion wave in a case of SBS. We have shown that in addition to the ion wave excited by the direct SBS of the pump and the seed pulse, there is another ion wave excited by SBS through an intermediate step involving a SRS. It has been shown for instance by Shoucri *et al.* (2015) in an un-magnetized plasma, that the problem of a SBS can only be solved by a Vlasov code, because of the intrinsic numerical noise associated with PIC codes. Finally, we have also presented in Section 6 an example of the application of this code to the problem of a wakefield accelerator in a magnetized plasma.

ACKNOWLEDGEMENTS

M. Shoucri is grateful to Dr. Réjean Girard for his constant interest and support. The author is grateful to the Centre de Calcul Scientifique de l'IREQ (CASIR) for the computer time used in the simulations presented in the present work.

REFERENCES

Andreev, A., Riconda, C., Tikhonchuk, V. & Weber, S. (2006). Short light pulse amplification and compression by stimulated Brillouin in plasmas in the strong coupling regime. *Phys. Plasmas* **13**, 053110/1–5.

Briand, C. (2015). Langmuir waves across the heliosphere. *J. Plasma Phys*. **81**, 1–27.

Denavit, J. & Sudan, R.N. (1975). Whistler sideband instability. *Phys. Fluids* **18**, 575–584.

Ghizzo, A., Bertrand, P., Shoucri, M., Johnston, T.W., Fijalkow, E. & Feix, M. (1990). A Vlasov code for the numerical solution of stimulated Raman scattering. *J. Comput. Phys*. **90**, 431–457.

Ghizzo, A., Bertrand, P., Shoucri, M., Johnston, T.W., Fijalkow, E., Feix, M. & Demchenko, V.V. (1992). Study of laser-plasma beat wave current drive with an Eulerian Vlasov code. *Nucl. Fusion* **32**, 45–65.

Grulke, O., Buttenschön, B. & Fahrenkamp, N. (2015). A high density helicon discharge for the advanced plasma accelerators AWAKE. *42nd EPS Conf. Plasma Physics*, Lisbonne P2.208.

Humphrey, K.A., Trines, R.M.G.M., Fiuza, F., Speirs, D.C., Norreys, P., Cairns, R.A., Silva, L.O. & Bingham, R. (2013). Effect of collisions on amplification of laser beams by Brillouin scattering in plasmas. *Phys. Plasmas* **20**, 102114/1–4.

Lancia, L., Marquès, J.-R., Nakatsutsumi, M., Riconda, C., Weber, S., Hüller, S., Mancic, A., Antici, P., Tikhonchuk, V.T., Héron, A., Audebert, P. & Fuchs, J. (2010). Experimental evidence of short light amplification using strong-coupling stimulated Brillouin scattering in the pump depletion regime. *Phys. Rev. Lett*. **104**, 025001/1–4.

Lehmann, G., Schluck, F. & Spatschek, K.H. (2012). Regions for Brillouin seed pulse growth in relativistic laser-plasma interaction. *Phys. Plasmas* **19**, 093120.

Lehmann, G. & Spatschek, K.H. (2013). Nonlinear Brillouin amplification of finite-duration seeds in the strong coupling regime. *Phys. Plasmas* **20**, 073112/1–10.

Lehmann, G., Spatschek, K.H. & Sewell, G. (2013). Pulse shaping during Raman-seed amplification for short laser pulses. *Phys. Rev. E* **87**, 063107/1–9.

Malkin, V.M. & Fisch, N.J. (2014). Key plasma parameters for resonant backward Raman amplification in plasma. *Eur. Phys. J. Spec. Top*. **223**, 1157.

Malkin, V.M., Shvets, G. & Fisch, N.J. (1999). Fast compression of laser beams to highly overcritical powers. *Phys. Rev. Lett*. **82**, 4448–44451.

Montgomery, D.S., Albright, B.J., Barnak, D.H., Chang, P.Y., Davies, J.R., Fiksel, G., Froula, D.H., Kline, J.L., MacDonald, M.J., Sefkow, A.B., Yin, L. & Betti, R. (2015). Use of external magnetic fields in hohlraum plasmas to improve laser-coupling. *Phys. Plasmas* **22**, 010703/1–13.

Mourou, G.A., Fisch, N.J., Malkin, V.M., Toroker, Z., Khazanov, A., Sergeev, M., Tajima, T. & Le Garrec, B. (2012). Exawatt-Zetawatt pulse generation and applications. *Opt. Commun*. **285**, 720.

Riconda, C., Weber, S., Lancia, L., Marques, J.R., Mourou, G.A. & Fuchs, J. (2013). Spectral characteristics of ultra-short laser pulses in plasma amplifiers. *Phys. Plasmas* **20**, 083115.

Shoucri, M. (2008*a*). *Numerical Solution of Hyperbolic Differential Equations*. N.Y.: Nova Science Publisher.

Shoucri, M. (2008*b*). Numerical simulation of wake-field acceleration using an Eulerian Vlasov code. *Commun. Comput. Phys*. **4**, 703–718.

Shoucri, M. & Storey, L.R.O. (1986). Motion of an electron bunch through a plasma. *Phys. Fluids* **29**, 262.

Shoucri, M., Matte, J.-P. & Vidal, F. (2014). A Vlasov code simulation of plasma-based backward Raman amplification in underdense plasma. *41rst EPS Conf. Plasma Physics*, Berlin, P5.093.

Shoucri, M., Matte, J.-P. & Vidal, F. (2015). Relativistic Eulerian Vlasov simulations of the amplification of seed pulses by Brillouin backscattering in plasmas. *Phys. Plasmas* **22**, 053101/1–13.

Summers, D., Tang, R., Omura, Y. & Lee, D. (2013). Parameter spaces for linear and nonlinear whistler-mode waves. *Phys. Plasmas* **20**, 072110/1–10.

Strozzi, D., Perkins, L.J., Marinak, M.M., Larson, D.J., Koning, J.M. & Logan, B.G. (2015). Imposed magnetic field and hot electron propagation in inertial fusion hohlraums. *J. Plasma Phys*. **81**, 475810603/1–21.

Tejero, E.M., Crabtree, C., Blackwell, D.D., Amatucci, W.E., Mithaiwala, M., Ganguli, G. & Rudakov, L. (2015). Laboratory studies of nonlinear wave processes in the Van Allen radiation belts. *Phys. Plasmas* **22**, 091503/1–7.

Toroker, Z., Malkin, V.M. & Fisch, N.J. (2014). Backward Raman amplification in the Langmuir wavebreaking regime. *Phys. Plasmas* **21**, 113110/1–10.

Trines, R.M.G.M., Fiuza, F., Bingham, R., Fonseca, R.A., Silva, L.O., Cairns, R.A. & Norreys, P.A. (2011). Simulations of efficient Raman amplification into the multipetawatt regime. *Nat. Phys*. **7**, 87.

Wang, T., Clark, D., Strozzi, D., Wilks, S., Martins, S. & Kirkwood, R. (2010). Particle-in-cell simulations of kinetic effects in plasma-based backward Ramam amplification in underdense plasmas. *Phys. Plasmas* **17**, 023109/1–9.

Weber, S., Riconda, C., Lancia, L., Marques, J.-R., Mourou, G.A. & Fuchs, J. (2013). Amplification of ultra-short laser pulses by Brillouin backscattering in plasmas. *Phys. Rev. Lett*. **111**, 055004.

https://doi.org/10.1017/S0263034616000185 Published online by Cambridge University Press